Supplement of Atmos. Chem. Phys., 26, 6321–6350, 2026
https://doi.org/10.5194/acp-26-6321-2026-supplement

Atmospheric Chemistry and Physics
Open Access
EGU

Supplement of

Vegetation drag partition effects redistribute dust globally

Siqing Xu et al.

Correspondence to: Siqing Xu (siqing.xu@lsce.ipsl.fr)

Section S1. Evaluation of threshold velocity in this study against the observationally retrieved threshold by Pu et al. (2020)

For the evaluation of the threshold velocity (u_t) in this study, we utilized the observationally retrieved 10-m wind speed threshold ($V_{threshold}$) based on dust aerosol optical depth (DAOD) from Pu et al. (2020). Specifically, we employed the version calculated using a DAOD criterion—0.5 for arid regions and 0.05 for semi-arid regions—to identify active dust emission events (Pu et al., 2020). To ensure a consistent point-to-point comparison, threshold velocity (u_t) used in this study with an original spatial resolution of 2.5° longitude × 1.27° latitude, was regridded to the 0.5° × 0.5° spatial resolution of the observational dataset (Fig. S2a–c) using a bilinear interpolation approach.

A comparison with satellite-retrieved thresholds ($V_{threshold}$) (Pu et al., 2020) showed that u_t has an overall alignment with $V_{threshold}$ in major desert regions, such as North Africa and Middle East, but exhibited much higher values in vegetated secondary sources, such as North America and southern Africa, especially when the vegetation effect is considered (Fig. S2d–e).

The discrepancy between the threshold velocity (u_t) used in this study and the satellite-retrieved ($V_{threshold}$) from Pu et al. (2020) primarily reflects fundamental differences in methodological definitions. In our scheme, u_t is determined from soil properties and a physically based parameterization of vegetation effects, representing the local conditions required for dust emission. In contrast, $V_{threshold}$ is inferred from dust aerosol optical depth (DAOD) associated with dust events. Because DAOD integrates contributions from both local emissions and dust transported from distant sources, it may not exclusively reflect local emission processes. The diagnostic utility of DAOD in representing local emission sources remains a subject of ongoing discussion. For example, some recent studies (Chappell et al., 2023) show limited correlation of DAOD with observed dust point sources (DPS), whereas others (Mahowald et al., 2024) argue that such discrepancies may result from the spatial and temporal scales of the satellite observations rather than a lack of physical connection. Consequently, the divergence between $V_{threshold}$ and adjusted u_t in this study underscores the inherent challenge of reconciling local-scale surface dynamics with column-integrated atmospheric constraints.

Section S2. Discussion of model–observation discrepancies in DAOD

Several seasonal and regional discrepancies are evident in the simulated DAOD compared to the observational dataset (Figs. 6 and 7), indicating that regional emission rescaling alone cannot fully correct model–observation differences. These biases arise from multiple sources, including uncertainties in dust emission representation, transport efficiency, and vertical mixing processes that collectively control the column-integrated dust loading.

The dust–climate interactions were decoupled in this study (Sect. 2.3.2), thereby suppressing radiative heating feedbacks from dust aerosols that are known to strengthen the African Summer Monsoon circulation (Balkanski et al., 2021). The resulting weakening of monsoon dynamics reduces surface wind intensity over key source regions such as Mali/Niger and Bodele/Sudan during JJA, thereby limiting dust emission strength. This dynamical suppression also affects downstream transport, reducing the export of dust toward the African West Coast and mid-Atlantic (Pope et al., 2016), and contributing to the observed underestimation in these regions.

In addition, the model likely underrepresents mesoscale convective systems and their associated cold-pool outflows, which are important drivers of intense dust emission events such as haboobs (Bergametti et al., 2022). These sub-grid convective gusts are particularly active during the pre-monsoon and early monsoon periods (May–June), when surface soils are most erodible due to limited vegetation cover. Their absence may further contribute to the negative DAOD bias in monsoon-influenced regions.

Similar to the patterns observed in North Africa, the simulated DAOD in the southern Middle East also exhibits underestimation during MAM and JJA, when this region is partly affected by the tropical monsoon (An et al., 2015). This further supports that monsoon-related biases are associated with deficiencies in large-scale circulation and convective dust emission processes, including the decoupling of dust-climate interactions (Balkanski et al., 2021), and unresolved haboob-scale convection (Pope et al., 2016; Bergametti et al., 2022).

In arid inland regions, the decoupling of dust-climate interactions may also reduce effective surface wind forcing and weaken long-range transport efficiency. This may lead to insufficient export of Asian dust and excessive near-source retention (Kok et al., 2021b), resulting in artificially enhanced local DAOD, as seen in the Kyzyl Kum desert during MAM and JJA, and Gobi during JJA (Fig. 7).

In contrast, the underestimation of DAOD in Taklamakan Desert especially during both MAM and DJF suggests a common model deficiency in resolving the vertical lofting of dust within this topographically enclosed basin (Nan and Wang, 2018). Strong terrain confinement and atmospheric stability restrict vertical lofting, leading to reduced column-integrated dust loading. During cold seasons, weaker vertical mixing further suppresses uplift, while in transition seasons the model might fail to fully represent episodic vertical transport, contributing to a systematic negative bias in DAOD.

Section S3. Model–Observation discrepancies in dust surface concentration

The downwind region of dust emission hotspots (e.g., sites over Japan in Fig. 2b, Fig. 9), the 4-mode configuration exhibits a more pronounced overestimation compared to the 1-mode. This discrepancy likely stems from the competing effects of massive initial emission and rapid gravitational settling of coarse particles. Although the 4-mode setup includes the 5–10 μm fractions that typically dominate observed spring dust events in Japan (Uematsu et al., 2003), the model may over-specify their initial mass flux. Because Japan is relatively close to Asian dust sources, the high surface concentrations might be driven by a massive initial emission flux that outpaces the removal rate over relatively short transport distances. While the 1-mode configuration's focus on finer dust fractions (MMD=2.5 μm) inherently omits dominant coarse particles, its closer agreement with observations appears physically fortuitous. Specifically, the slower settling velocity of the 2.5 μm dust fraction may artificially extend particle residence time to mask deficiencies in transport efficiency or an overestimation of emission. Ultimately, these systematic differences underscore that downwind dust concentrations are governed by the interplay between particle size representation and atmospheric lifetime, rather than emission strength alone.

Section S4. Analysis of persistent overestimation of dust deposition in Antarctica

Regarding the Southern Hemisphere, the persistent overestimation of dust surface total deposition over Antarctica—a common feature in global models (Leung et al., 2024)—likely reflects unresolved topographic and boundary-layer processes. Unlike the highly heterogeneous alpine terrain, where steep peaks can cause sub-grid elevation mismatches (Sect. 2.3.5), the Antarctic interior consists of a vast, relatively homogeneous plateau with a model-represented average elevation of approximately 2000 m (mean elevation south of 70° S is 1952 m), basically aligning with the description of a high-altitude plateau exceeding 2000 m (Tewari et al., 2021). The stations on this plateau remain within the shallow boundary layer resolved by the model and can thus be reasonably compared with simulated surface deposition. However, while the model captures the broad plateau elevation, it may not resolve fine-scale katabatic winds confined to this shallow, stably stratified layer, which regulate near-surface transport and dust divergence toward the coast. Coarse-resolution models cannot fully represent these flows, likely underestimating seaward export and enhancing inland deposition.

Table S1. Target and original emission from the vegetation-impact simulation in 1-mode configuration prior to rescaling at the year of 2008, along with the corresponding rescaling factors applied in the nine regions.

Regions	Target dust emission (Tg yr^{-1})	Original dust emission (Tg yr^{-1})	Rescaling factors
Western North Africa	314	448	0.7
Eastern North Africa	257	397	0.6
The Sahel	200	242	0.8
The Middle East*	210	79	2.7
Central Asia*	283	106	2.7
East Asia	207	365	0.6
North America	46	2	23.2
Australia	57	38	1.5
South America	68	1	82.0
Southern Africa	36	1	62.0

*Note: To provide a more detailed regional characterization, the Middle East and central Asia (originally aggregated in Kok et al. (2021a), Fig. S5) were differentiated: The Middle East is defined as the region situated south of 40°N and west of 60°E, and the remaining areas of the original domain, are categorized as central Asia.

Table S2. Global mean annual Dust Aerosol Optical Depth (DAOD) and statistical performance metrics for simulated DAOD, surface PM concentration, and dust deposition. Results are shown for both control and vegetation-impact simulations in the 1-mode and 4-mode configurations with different scaling coefficients for all data points. For 4-mode, the scaling coefficient refers to the Mode 2 and Mode 3, which is the same for both modes.

		1-mode		4-mode		1-mode		4-mode		4-mode		4-mode	
		Control	Vegetation-impact	Control	Vegetation-impact	Control	Vegetation-impact	Control	Vegetation-impact	Control	Vegetation-impact	Control	Vegetation-impact
Scaling coefficient		1		1		0.74		1.24		1.44		1.51	
Global mean annual DAOD		0.042	0.034	0.026	0.021	0.031	0.025	0.031	0.025	0.035	0.028	0.037	0.030
DAOD vs AERONET-SDA	R^2	0.68	0.63	0.68	0.68	0.68	0.63	0.67	0.68	0.67	0.68	0.67	0.68
	RMSE	0.16	0.13	0.07	0.05	0.09	0.07	0.10	0.07	0.13	0.09	0.14	0.09
	MB	0.13	0.09	0.03	0.00	0.06	0.03	0.06	0.03	0.09	0.05	0.10	0.06
	Slope	0.48	0.51	0.73	0.87	0.64	0.69	0.61	0.73	0.53	0.64	0.51	0.62
DAOD vs Kok et al. (2021a)	R^2	0.53	0.59	0.48	0.54	0.53	0.59	0.48	0.54	0.48	0.54	0.48	0.54
	RMSE	0.16	0.12	0.10	0.09	0.10	0.08	0.11	0.09	0.14	0.10	0.14	0.11
	MB	0.07	0.04	-0.01	-0.03	0.02	-0.01	0.02	0.00	0.04	0.02	0.05	0.02
	Slope	0.42	0.51	0.60	0.74	0.57	0.69	0.50	0.62	0.44	0.55	0.42	0.53
Dust surface concentration evaluation	R (log)	0.90	0.91	0.89	0.90	0.90	0.91	0.89	0.90	0.89	0.90	0.89	0.90
	RMSE (log)	0.45	0.43	0.50	0.51	0.44	0.45	0.51	0.50	0.53	0.51	0.54	0.51
	MB (log)	0.11	0.01	0.02	-0.09	-0.02	-0.12	0.11	0.00	0.17	0.06	0.19	0.08
Dust surface total deposition evaluation	R (log)	0.84	0.86	0.81	0.83	0.84	0.86	0.81	0.83	0.81	0.83	0.81	0.83
	RMSE (log)	0.77	0.70	0.86	0.80	0.74	0.69	0.90	0.82	0.93	0.84	0.94	0.85
	MB (log)	0.27	0.14	0.31	0.17	0.14	0.01	0.39	0.26	0.45	0.32	0.47	0.34

Table S3. Summary of statistics (R^2, R, RMSE, NRMSE, and MB) for the model evaluation, including dust emission, DAOD, dust surface PM concentration and total deposition, in the control and vegetation-impact simulations, using the 1-mode and 4-mode configurations, respectively. Statistics for DAOD, surface PM, and deposition are calculated only for grid cells where the relative difference between control and vegetation-impact simulations exceeds 3 % (or 5 %), consistent with the thresholds applied in Figs. 6, 7, 9, 11, S22, and S26.

Variables	Size-mode	Simulation	R^2	R	RMSE	NRMSE	MB
Emission against DustCOMM by Kok et al., 2021b	1-mode	Control	0.87	0.93	57.58	42 %	39.86
		Vegetation-impact	1.00	1.00	0.18	0 %	0.01
	4-mode	Control	0.86	0.93	551.15	43 %	387.09
		Vegetation-impact	0.99	1.00	94.57	7 %	0.13
DAOD against AERONET-SDA	1-mode	Control	0.68	0.82	0.09	66 %	0.06
		Vegetation-impact	0.63	0.80	0.07	53 %	0.03
	4-mode	Control	0.67	0.82	0.10	71 %	0.06
		Vegetation-impact	0.68	0.83	0.07	49 %	0.03
DAOD against model constraints by Kok et al., 2021a	1-mode	Control	0.52	0.72	0.10	73 %	0.02
		Vegetation-impact	0.57	0.76	0.09	60 %	0.00
	4-mode	Control	0.47	0.68	0.12	83 %	0.02
		Vegetation-impact	0.53	0.73	0.09	65 %	0.00
Surface PM concentration against Mahowald et al., 2009	1-mode	Control	0.81 (log space)	0.90 (log space)	0.44 (log space)	10 % (log space)	-0.02 (log space)
		Vegetation-impact	0.82 (log space)	0.91 (log space)	0.45 (log space)	10 % (log space)	-0.12 (log space)
	4-mode	Control	0.83 (log space)	0.91 (log space)	0.51 (log space)	12 % (log space)	0.15 (log space)
		Vegetation-impact	0.84 (log space)	0.92 (log space)	0.49 (log space)	12 % (log space)	0.03 (log space)
Surface deposition against Albani et al. (2014)	1-mode	Control	0.66 (log space)	0.81 (log space)	0.80 (log space)	14 % (log space)	0.15 (log space)
		Vegetation-impact	0.70 (log space)	0.84 (log space)	0.74 (log space)	13 % (log space)	-0.01 (log space)
	4-mode	Control	0.59 (log space)	0.77 (log space)	0.96 (log space)	19 % (log space)	0.36 (log space)
		Vegetation-impact	0.64 (log space)	0.80 (log space)	0.87 (log space)	17 % (log space)	0.19 (log space)

Table S4. Global and regional dust emissions and their relative contributions under control and vegetation-impact simulations in the 1-mode configuration.

Regions	Dust emission (Tg yr^{-1})			Contribution of each region (%)	
	Control simulation	Vegetation-impact simulation	Relative reduction (%)	Control simulation	Vegetation-impact simulation
Global	1601	1243	22 %	——	
Western North Africa	234	233	1 %	15 %	19 %
Eastern North Africa	193	190	1 %	12 %	15 %
The Middle East*	166	155	7 %	10 %	13 %
East Asia	168	154	8 %	10 %	12 %
The Sahel	168	148	12 %	11 %	12 %
Central Asia*	298	210	30 %	19 %	17 %
Australia	64	42	34 %	4 %	3 %
South America	89	50	44 %	6 %	4 %
Southern Africa	59	27	55 %	4 %	2 %
North America	162	34	79 %	10 %	3 %

*Note: To provide a more detailed regional characterization, the Middle East and Central Asia (originally aggregated in Kok et al. (2021a), Fig. S5) were differentiated: The Middle East is defined as the region situated south of 40°N and west of 60°E, and the remaining areas of the original domain, are categorized as Central Asia.

Table S5. Global and regional dust emissions, DAOD, surface concentrations, and deposition rates for the control and vegetation-impact simulations in the 1-mode configuration. Relative reductions (%) between the two simulations are also provided.

	Dust emission (Tg yr^{-1})			DAOD			Surface PM concentration (μg m^{-3})			Surface total deposition (g m^{-2} yr^{-1})		
	Control	Vegetation-impact	Relative reduction (%)	Control	Vegetation-impact	Relative reduction (%)	Control	Vegetation-impact	Relative reduction (%)	Control	Vegetation-impact	Relative reduction (%)
Global	1601	1243	22 %	0.031	0.025	19 %	12	10	17 %	3	2	23 %
Western North Africa	234	233	1 %	0.249	0.238	4 %	117	115	2 %	20	19	4 %
Eastern North Africa	193	190	1 %	0.204	0.194	5 %	94	92	2 %	17	16	2 %
The Middle East*	166	155	7 %	0.155	0.139	11 %	63	59	7 %	14	13	8 %
East Asia	168	154	8 %	0.137	0.121	12 %	68	62	10 %	15	13	9 %
The Sahel	168	148	12 %	0.222	0.209	6 %	90	85	6 %	19	18	7 %
Central Asia*	298	210	30 %	0.201	0.160	20 %	90	69	23 %	26	23	13 %
Australia	64	42	34 %	0.026	0.017	34 %	15	10	33 %	3	2	34 %
South America	89	50	44 %	0.012	0.008	37 %	3	2	46 %	3	2	43 %
Southern Africa	59	27	55 %	0.026	0.015	43 %	10	5	47 %	4	2	52 %
North America	162	34	79 %	0.042	0.013	69 %	21	5	75 %	7	2	75 %

*Note: To provide a more detailed regional characterization, the Middle East and central Asia (originally aggregated in Kok et al. (2021a), Fig. S5) were differentiated: The Middle East is defined as the region situated south of 40°N and west of 60°E, and the remaining areas of the original domain, are categorized as central Asia.

Table S6. Global and regional dust emissions, DAOD, surface concentrations, and deposition rates for the control and vegetation-impact simulations in the 4-mode configuration. Relative reductions (%) between the two simulations are also provided.

	Dust emission (Tg yr^{-1})			DAOD			Surface PM_{10} concentration (μg m^{-3})			Surface PM_{10} total deposition (g m^{-2} yr^{-1})		
	Control	Vegetation-impact	Relative reduction (%)	Control	Vegetation-impact	Relative reduction (%)	Control	Vegetation-impact	Relative reduction (%)	Control	Vegetation-impact	Relative reduction (%)
Global	15058	11575	23 %	0.031	0.025	19 %	25	20	19 %	12	9	23 %
Western North Africa	2098	2082	1 %	0.255	0.247	3 %	254	251	1 %	112	108	4 %
Eastern North Africa	1768	1744	1 %	0.208	0.201	4 %	207	203	2 %	118	116	1 %
The Middle East*	1467	1363	7 %	0.148	0.133	10 %	121	112	7 %	70	65	7 %
East Asia	1556	1433	8 %	0.147	0.132	11 %	156	142	9 %	61	57	6 %
The Sahel	1518	1344	11 %	0.222	0.209	6 %	179	167	6 %	64	58	9 %
Central Asia*	2887	1957	32 %	0.214	0.168	21 %	207	153	26 %	115	96	16 %
Australia	626	409	35 %	0.028	0.019	35 %	32	21	34 %	14	9	35 %
South America	1263	720	43 %	0.020	0.012	40 %	13	7	47 %	26	15	42 %
Southern Africa	556	229	59 %	0.026	0.013	49 %	22	11	51 %	24	10	57 %
North America	1320	295	78 %	0.042	0.012	71 %	46	12	75 %	35	8	76 %

*Note: To provide a more detailed regional characterization, the Middle East and central Asia (originally aggregated in Kok et al. (2021a), Fig. S5) were differentiated: The Middle East is defined as the region situated south of 40°N and west of 60°E, and the remaining areas of the original domain, are categorized as central Asia.

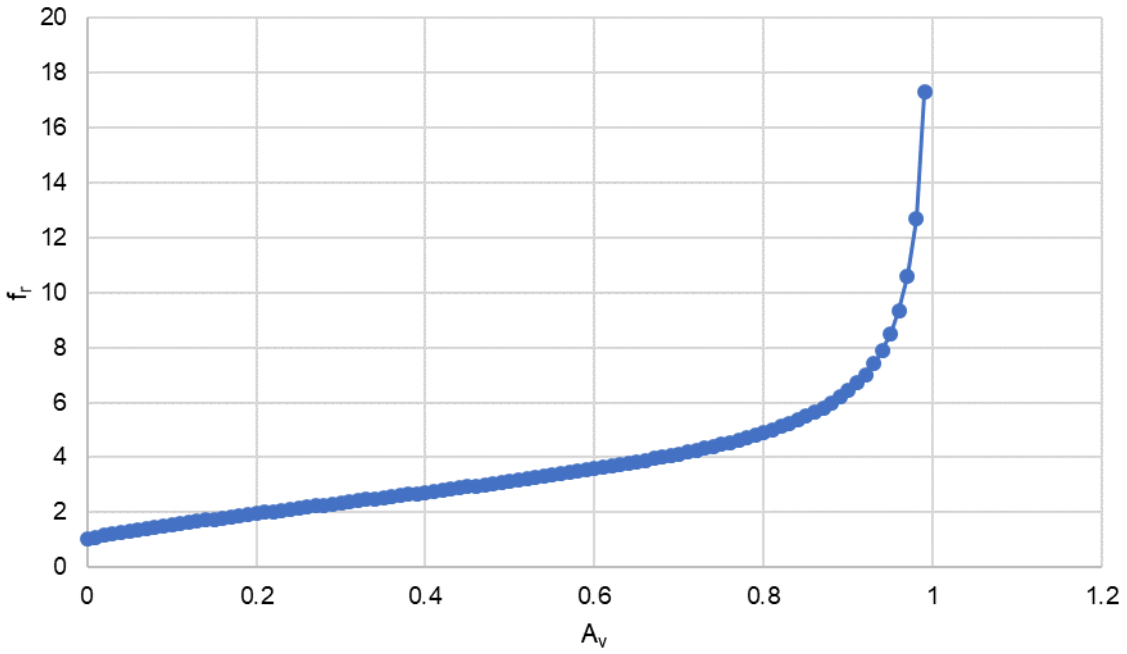

Figure S1. Relationship between the fraction of vegetation cover (A_v) and the correction factor related to surface roughness (f_r).

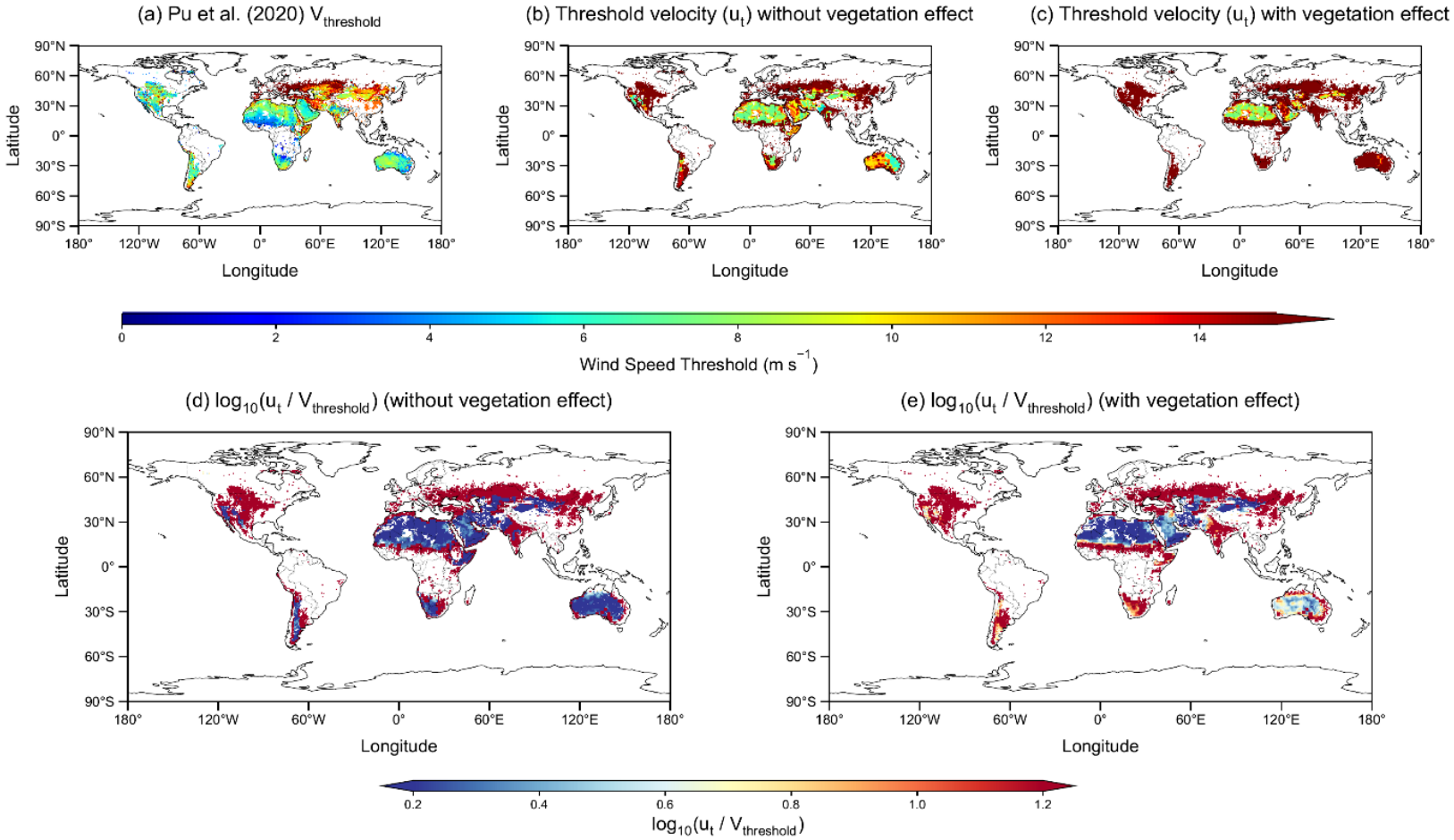

Figure S2. Comparison between observationally-retrieved and modelled dust emission threshold velocities. (**a**) Satellite-retrieved 10-m wind speed threshold ($V_{threshold}$) from Pu et al. (2020), using a high dust intensity threshold (DOD > 0.5) to identify active emission events. (**b**, **c**) Model-simulated threshold velocity (u_t) without and with the effect of vegetation, respectively. (**d**, **e**) Spatial distribution of the logarithmic ratio, $\log_{10}(u_t/V_{threshold})$, excluding and including vegetation effects. All model data were interpolated to a 0.5° × 0.5° spatial resolution to match the observational grid.

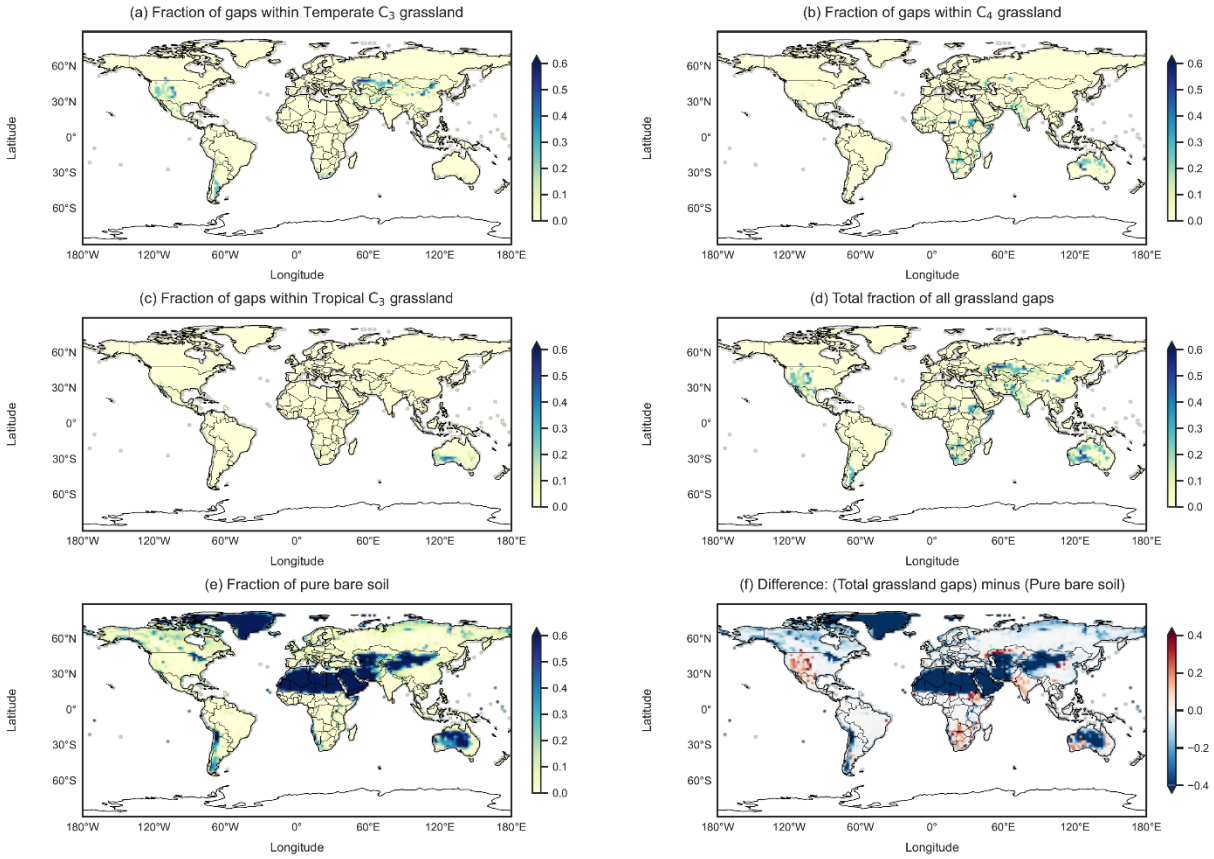

Figure S3. Global distribution of the bare soil fraction derived from ORCHIDEE averaged over 2004–2020. The fraction of bare soil gaps within (a) temperate C_3 grassland, (b) C_4 grassland, and (c) tropical C_3 grassland; (d) the total fraction of all bare soil in grassland gaps; (e) the fraction of pure bare soil; and (f) the difference between the total bare soil fraction in grassland gaps and the pure bare soil fraction.

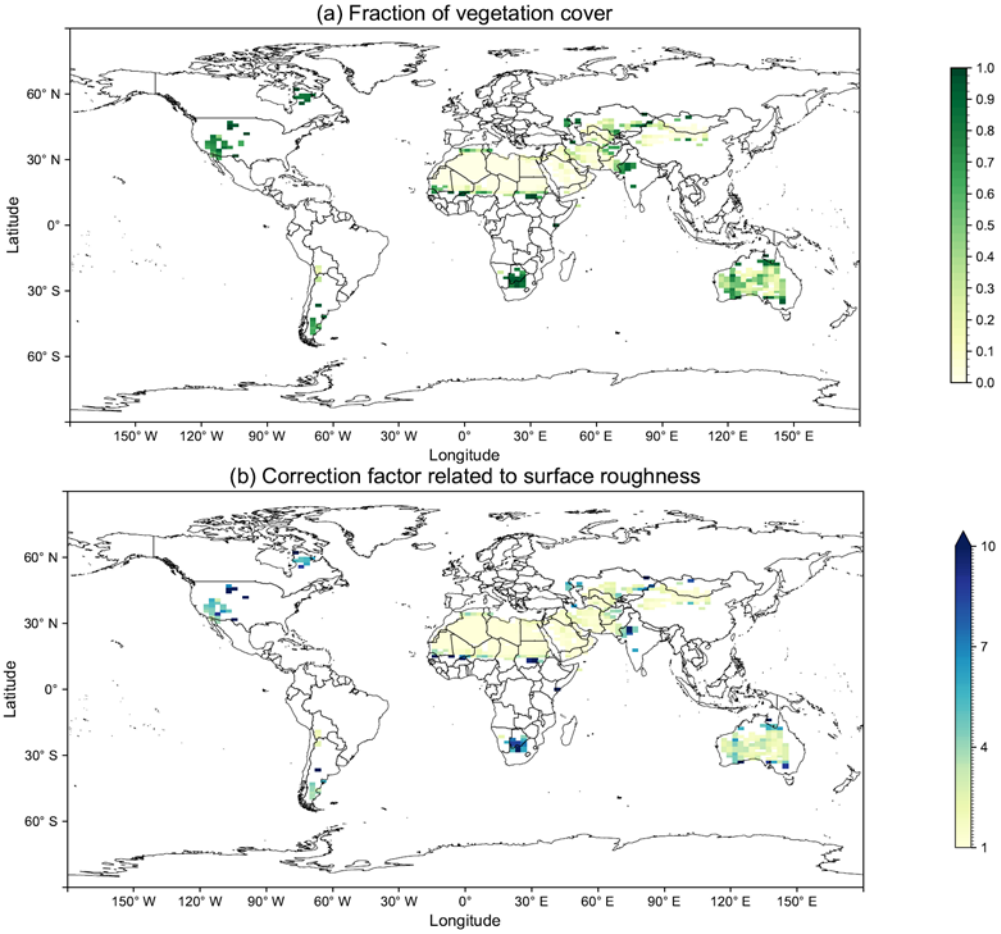

Figure S4. Global distribution of vegetation cover (A_v) and surface roughness correction factor (f_r), averaged over 2004–2020. (**a**) Fraction of vegetation cover (A_v). The A_v values, including the grasslands, forests, and croplands, are derived from the ORCHIDEE land surface model. (**b**) Correction factor related to surface roughness (f_r). The f_r values are parameterized based on the fraction of vegetation cover (A_v). In both panels, white color represents regions without valid data (e.g., oceans) or where the values fall outside the defined display range (e.g., f_r greater than 100). Both fields represent 17-year averages (2004–2020) and are shown only for grid cells where dust emission is permitted.

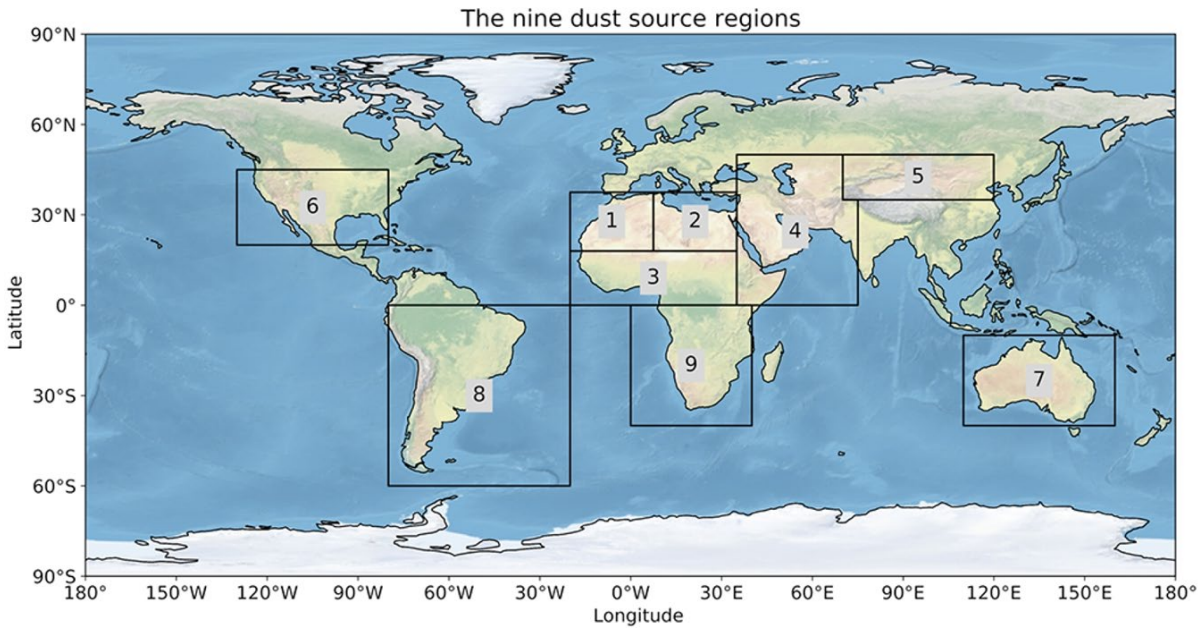

Figure S5. Geographical location of nine dust source regions. The nine regions include (1) western North Africa, (2) eastern North Africa, (3) the southern Sahara and Sahel, (4) the Middle East and central Asia (which includes the Horn of Africa), (5) East Asia, (6) North America, (7) Australia, (8) South America, and (9) southern Africa. The graph is taken from Kok et al. (2021a).

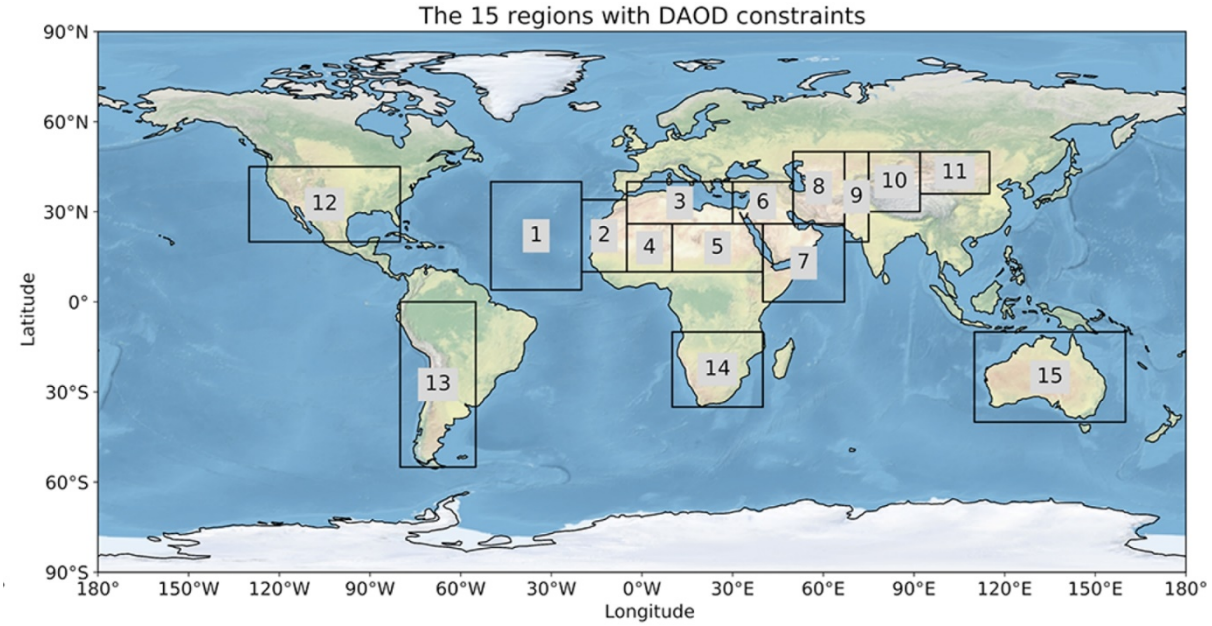

Figure S6. Geographical location of the 15 observed dusty regions. The regions include: (1) Mid-Atlantic, (2) African west coast, (3) Northern Africa, (4) Mali /Niger, (5) Bodélé / Sudan, (6) Northern Middle East, (7) Southern Middle East, (8) Kyzylkum, (9) Thar, (10) Taklamakan, (11) Gobi, (12) North America, (13) South America, (14) southern Africa, and (15) Australia. The graph is taken from Kok et al. (2021a).

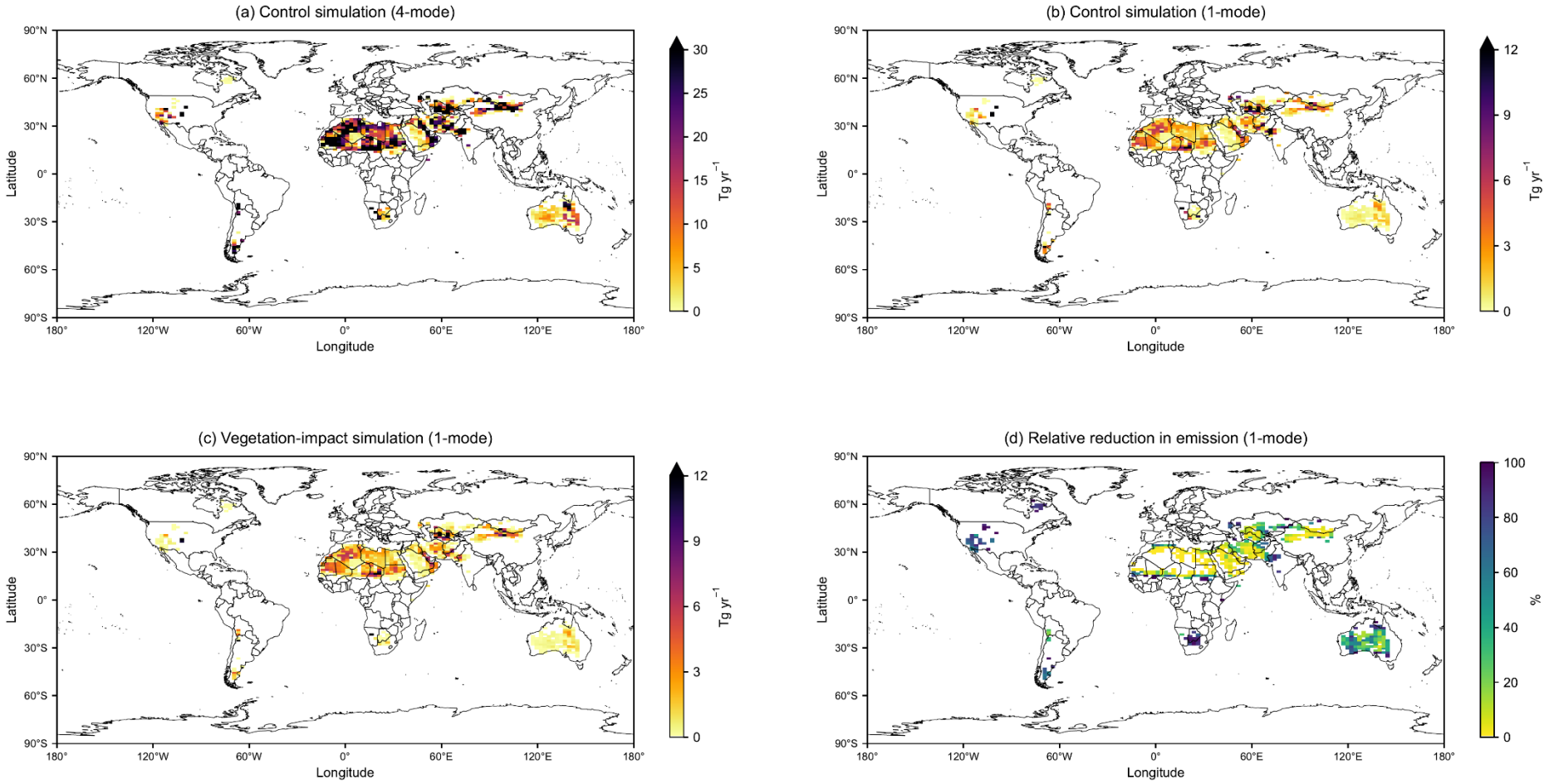

Figure S7. Simulated global dust emission fluxes and the quantified impact of vegetation. Mean annual dust emission flux (Tg yr^{-1}) in (**a**) the control simulation of the 4-mode configuration, and in (**b**, **c**) the control and vegetation-impact simulations of the 1-mode configuration, respectively. (**d**) Relative reduction in dust emission (%) due to vegetation in the 1-mode configuration, calculated as (control − vegetation-impact) / control.

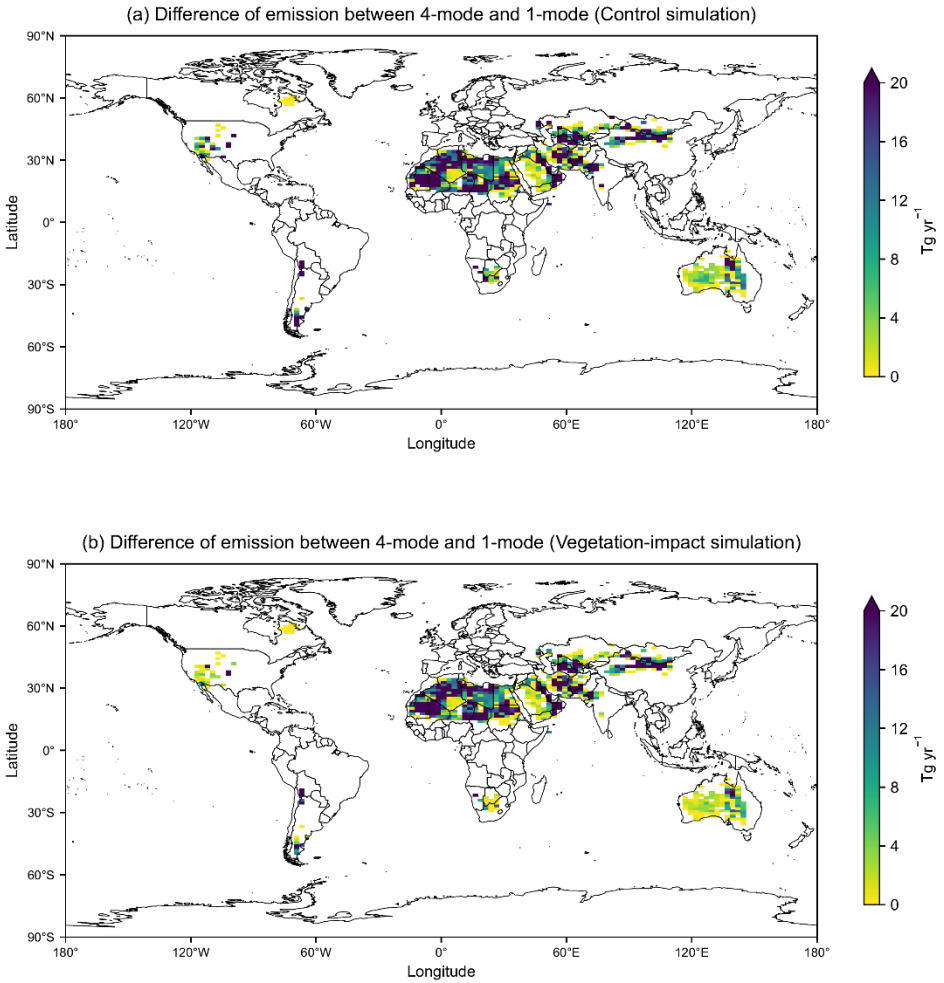

Figure S8. Difference in mean annual dust emission between the 4-mode and 1-mode configurations in the (**a**) control simulation and the (**b**) vegetation-impact simulation, calculated as 4-mode minus 1-mode.

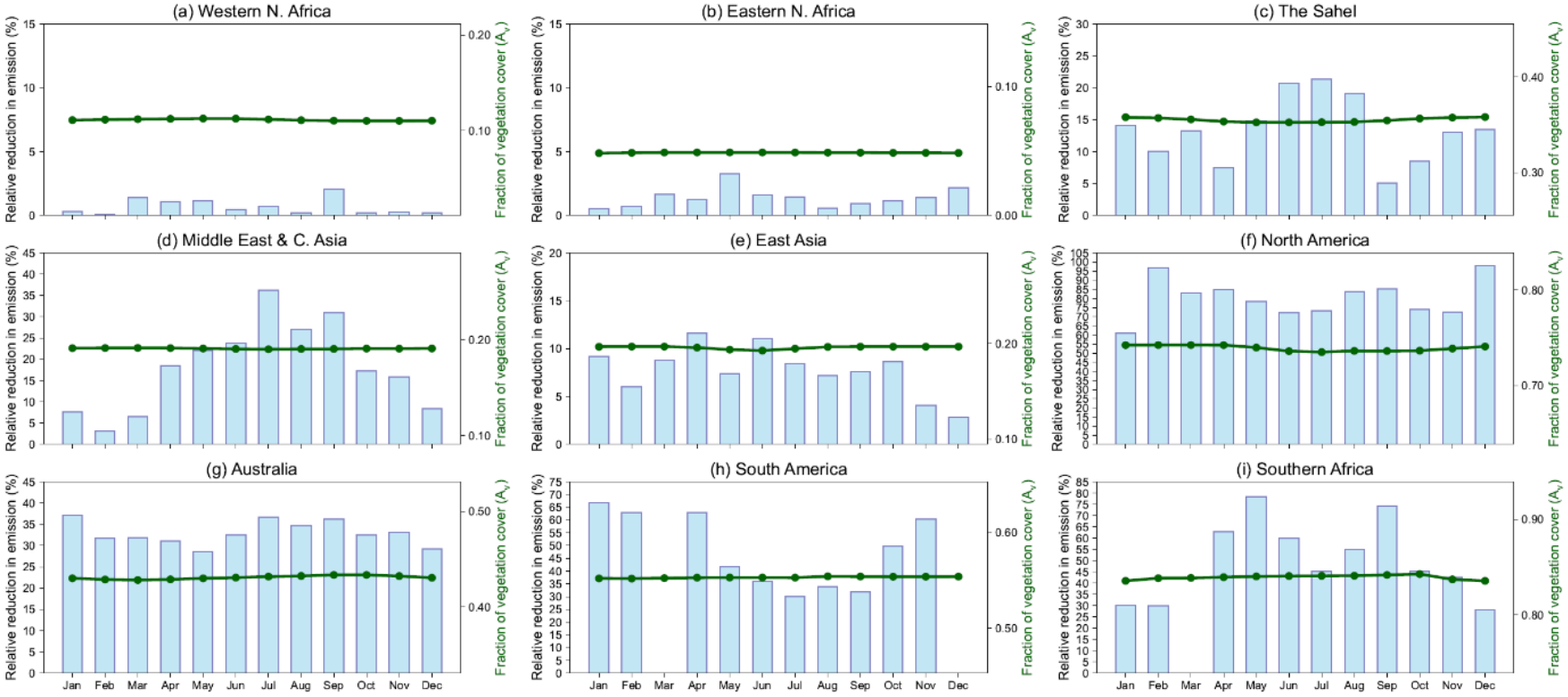

Figure S9. Seasonality of relative reduction in dust emission and fraction of vegetation cover (A_v) in the 1-mode configuration. Monthly variations are shown for nine dust-source regions: (**a**) Western North Africa, (**b**) Eastern North Africa, (**c**) the Sahel, (**d**) the Middle East and central Asia, (**e**) East Asia, (**f**) North America, (**g**) Australia, (**h**) South America, and (**i**) southern Africa. The left y-axis represents the relative reduction in emission (%), calculated as (Control−Vegetation-impact)/Control. The right y-axis represents the fraction of vegetation cover (A_v). Bars denote emission reduction, and the line with markers denotes the vegetation fraction.

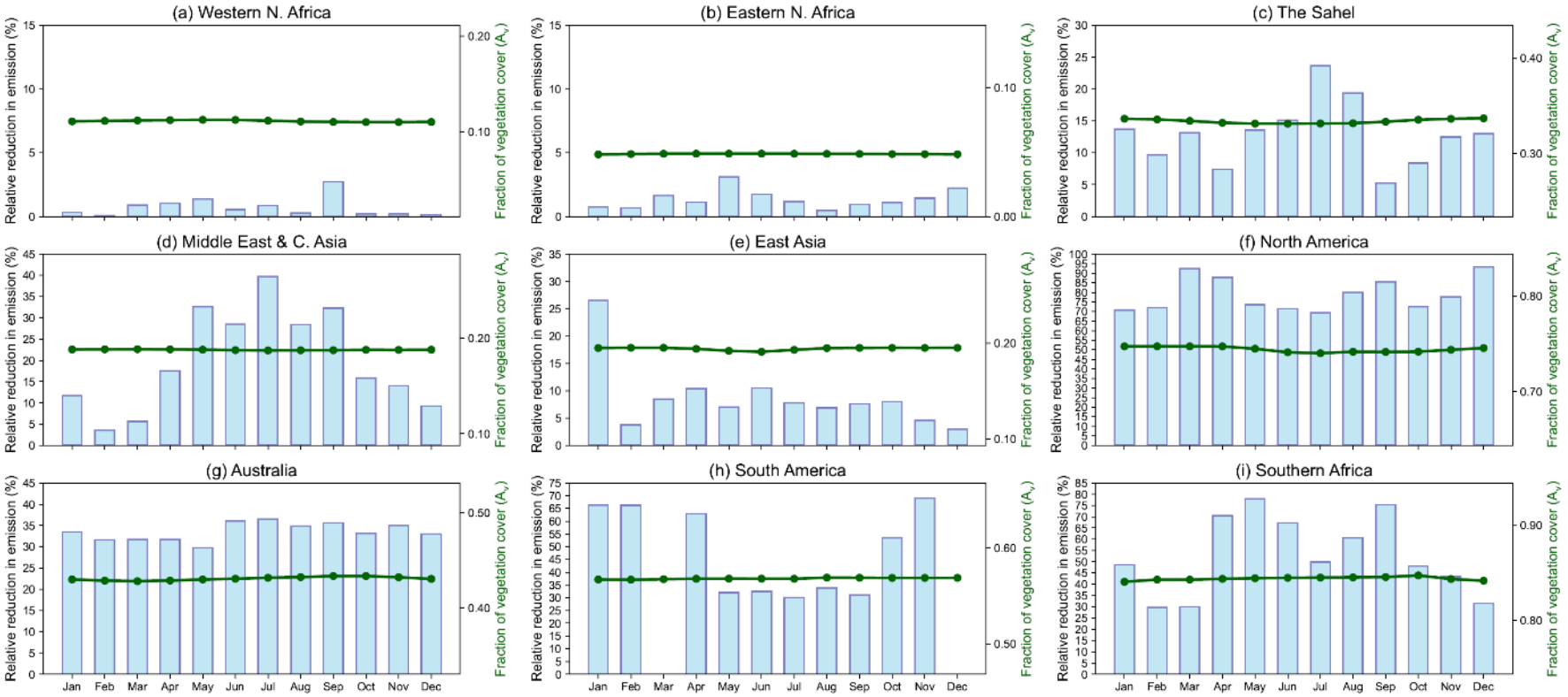

Figure S10. Seasonality of relative reduction in dust emission and fraction of vegetation cover (A_v) in the 4-mode configuration. Monthly variations are shown for nine dust-source regions: (**a**) Western North Africa, (**b**) Eastern North Africa, (**c**) the Sahel, (**d**) the Middle East and central Asia, (**e**) East Asia, (**f**) North America, (**g**) Australia, (**h**) South America, and (**i**) southern Africa. The left y-axis represents the relative reduction in emission (%), calculated as (Control−Vegetation-impact)/Control. The right y-axis represents the fraction of vegetation cover (A_v). Bars denote emission reduction, and the line with markers denotes the vegetation fraction.

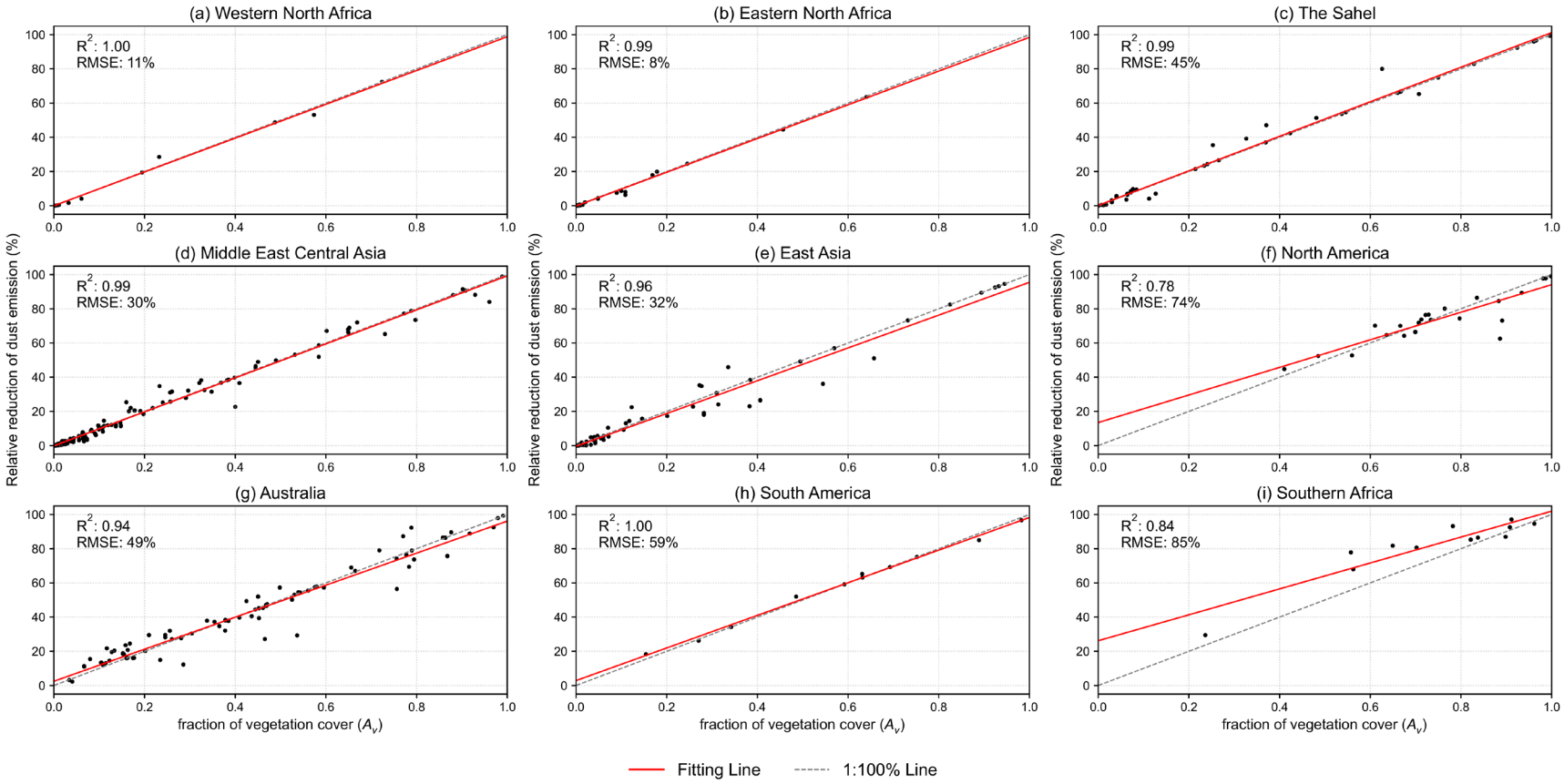

Figure S11. Relationship between the mean annual fraction of vegetation cover (A_v) and the relative reduction of dust emission in 1-mode configuration for nine dust source regions, including (**a**) Western North Africa, (**b**) Eastern North Africa, (**c**) the Sahel, (**d**) the Middle East and central Asia, (**e**) East Asia, (**f**) North America, (**g**) Australia, (**h**) South America, and (**i**) southern Africa. Each point represents a grid cell. The relative reduction is calculated as (control − vegetation-impact) / control.

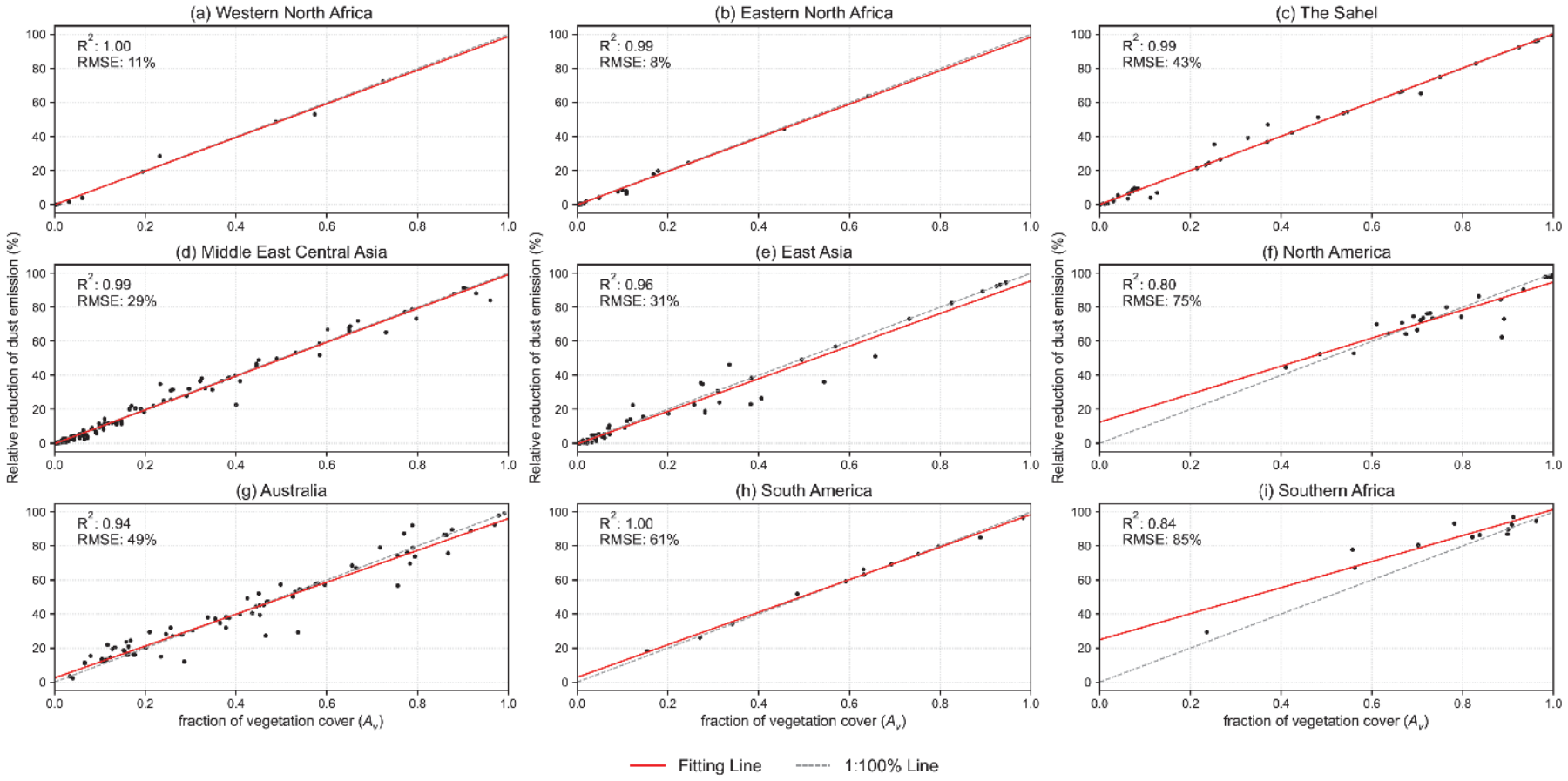

Figure S12. Relationship between the mean annual fraction of vegetation cover (A_V) and the relative reduction of dust emission in 4-mode configuration for nine dust source regions, including (**a**) Western North Africa, (**b**) Eastern North Africa, (**c**) the Sahel, (**d**) the Middle East and central Asia, (**e**) East Asia, (**f**) North America, (**g**) Australia, (**h**) South America, and (**i**) southern Africa. Each point represents a grid cell. The relative reduction is calculated as (control − vegetation-impact) / control.

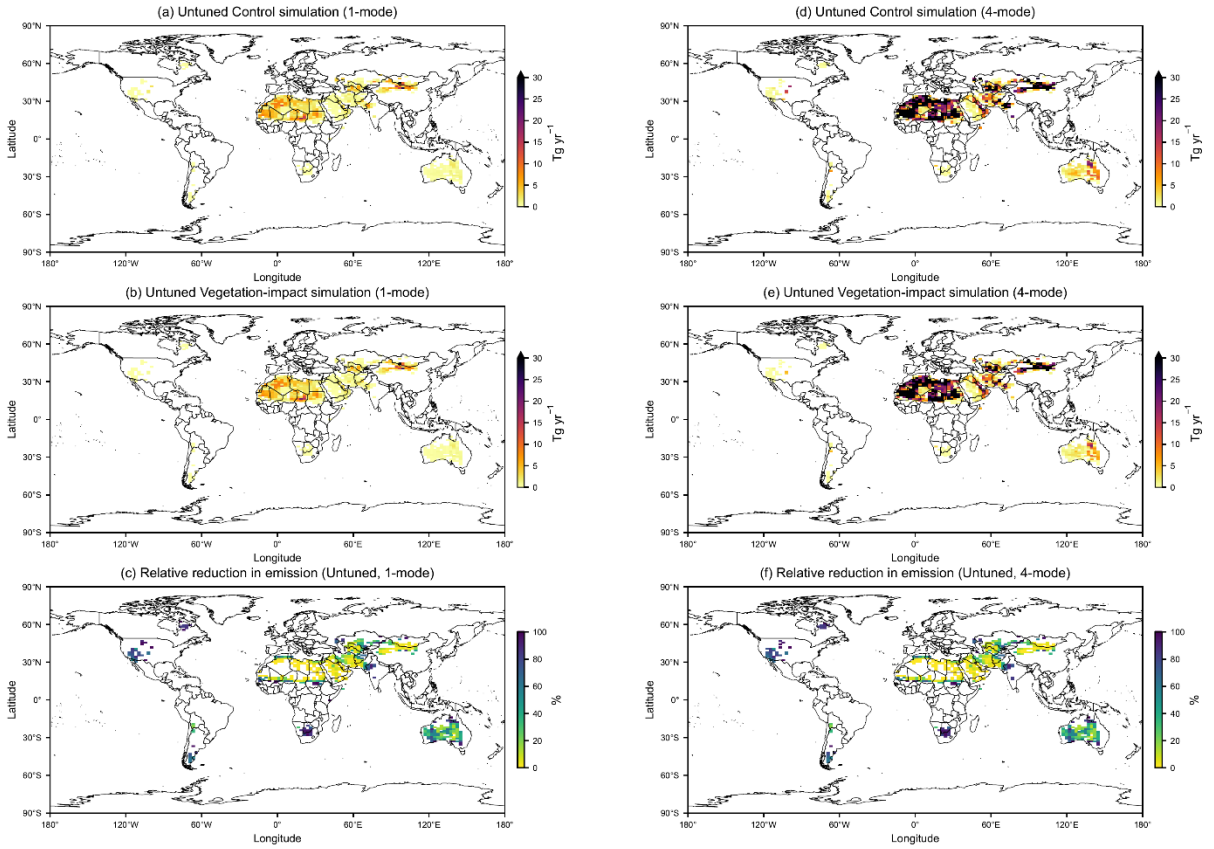

Figure S13. Simulated global mean annual dust emission fluxes (Tg yr^{-1}) without regional rescaling. Panels (a–b) and (d–e) show the control and vegetation-impact simulations for the 1-mode and 4-mode configurations, respectively. Panels (c) and (f) display the corresponding relative reduction in emission (%) due to vegetation, calculated as (control–vegetation-impact)/control, in the 1-mode and 4-mode configurations, respectively.

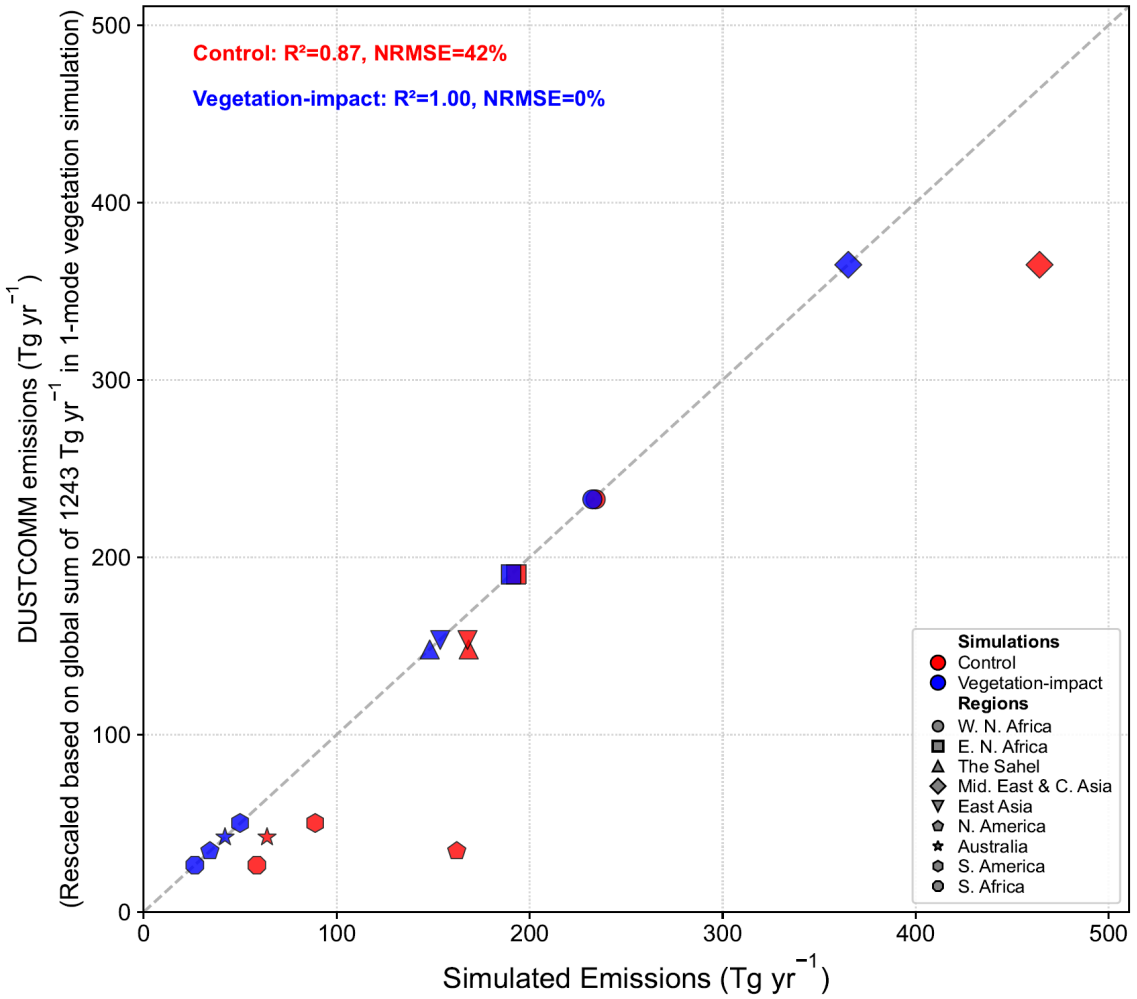

Figure S14. Comparison of simulated regional dust emissions (X-axis) against the DustCOMM emission by Kok et al. (2021b) (Y-axis) in 1-mode configuration. The rescaling factors were applied to both the control (red) and vegetation-impact (blue) simulations. The DustCOMM emissions were rescaled to the global total emissions in the vegetation-impact simulation. The 1:1 line, R^2, and NRMSE are provided for reference.

215

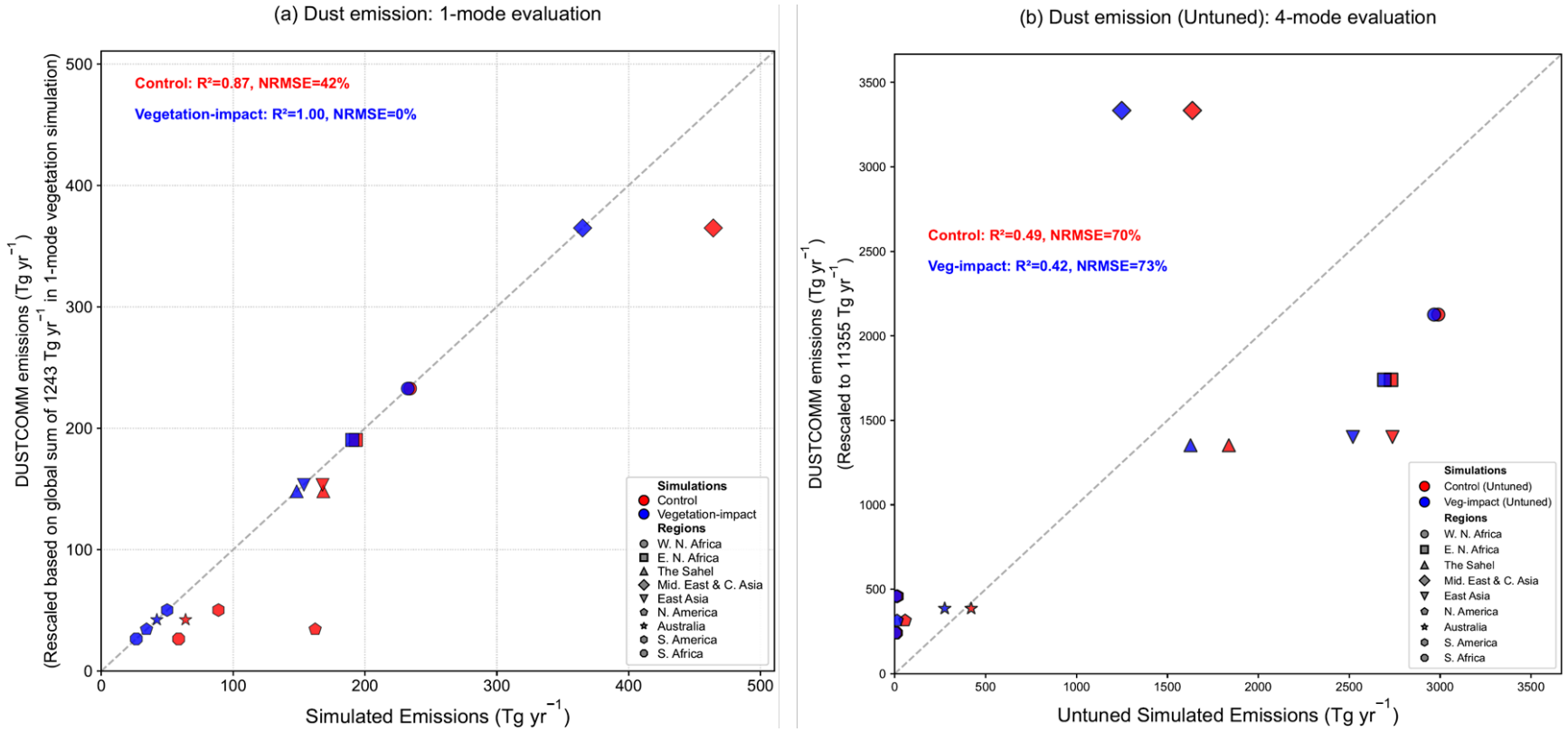

Figure S15. Regional evaluation of untuned simulated dust emissions against DustCOMM constraints (Kok et al., 2021b). Scatter plots for the (a) 1-mode and (b) 4-mode configurations compare emissions from the control (red) and vegetation-impact (blue) simulations without regional tuning. For direct comparison, DustCOMM emissions (y-axis) are rescaled to the global total of the untuned vegetation-impact simulation. The 1:1 line (dashed), R^2, and NRMSE are provided for reference.

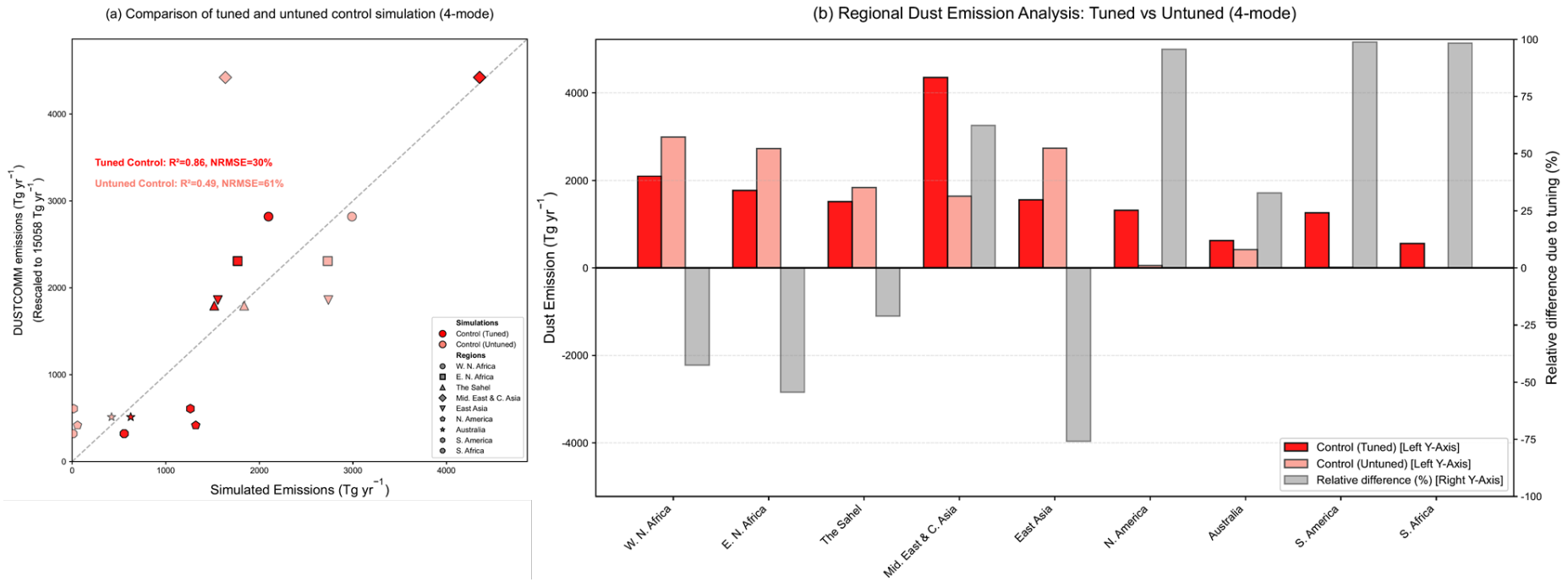

Figure S16. Comparison of tuned and untuned dust emission in the control simulation (4-mode configuration). (a) Regional evaluation of simulated dust emissions against DustCOMM constraints (Kok et al., 2021b) without (untuned; pink markers) and with (tuned; red markers) regional rescaling. The DustCOMM emissions were rescaled to the global total of the tuned control simulation for direct comparison. The 1:1 line (dashed), R^2, and NRMSE are provided for reference. (b) Regional dust emission magnitudes in tuned (red bars) and untuned (pink bars) control simulations (left Y-axis), and the corresponding relative difference due to tuning (grey bars; right Y-axis). The relative difference is calculated as (tuned−untuned)/tuned.

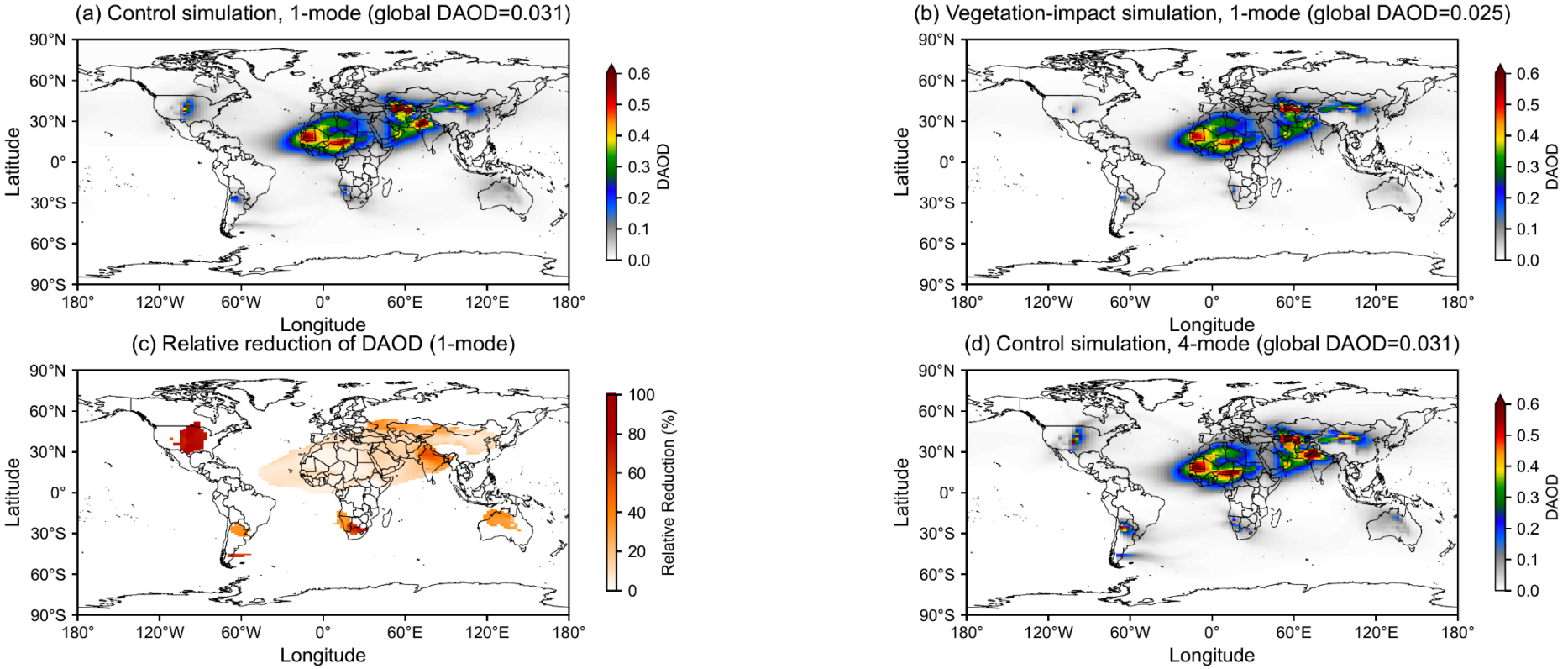

230 **Figure S17.** Spatial distribution of mean annual dust aerosol optical depth (DAOD) at 550 nm. Panels (**a**) and (**b**) show the control and vegetation-impact simulations using the 1-mode configuration, respectively. Panel (**c**) shows the relative difference between these two 1-mode simulations, calculated as (control − vegetation-impact) / control, with only grid cells with DAOD ≥ 0.05 displayed. Panel (**d**) presents the control simulation using the 4-mode configuration. The specific area-weighted global mean annual DAOD is indicated in panels **a**, **b**, **d**. All simulations incorporate scaling coefficients to match the observation-based target range of 0.030 ± 0.005.

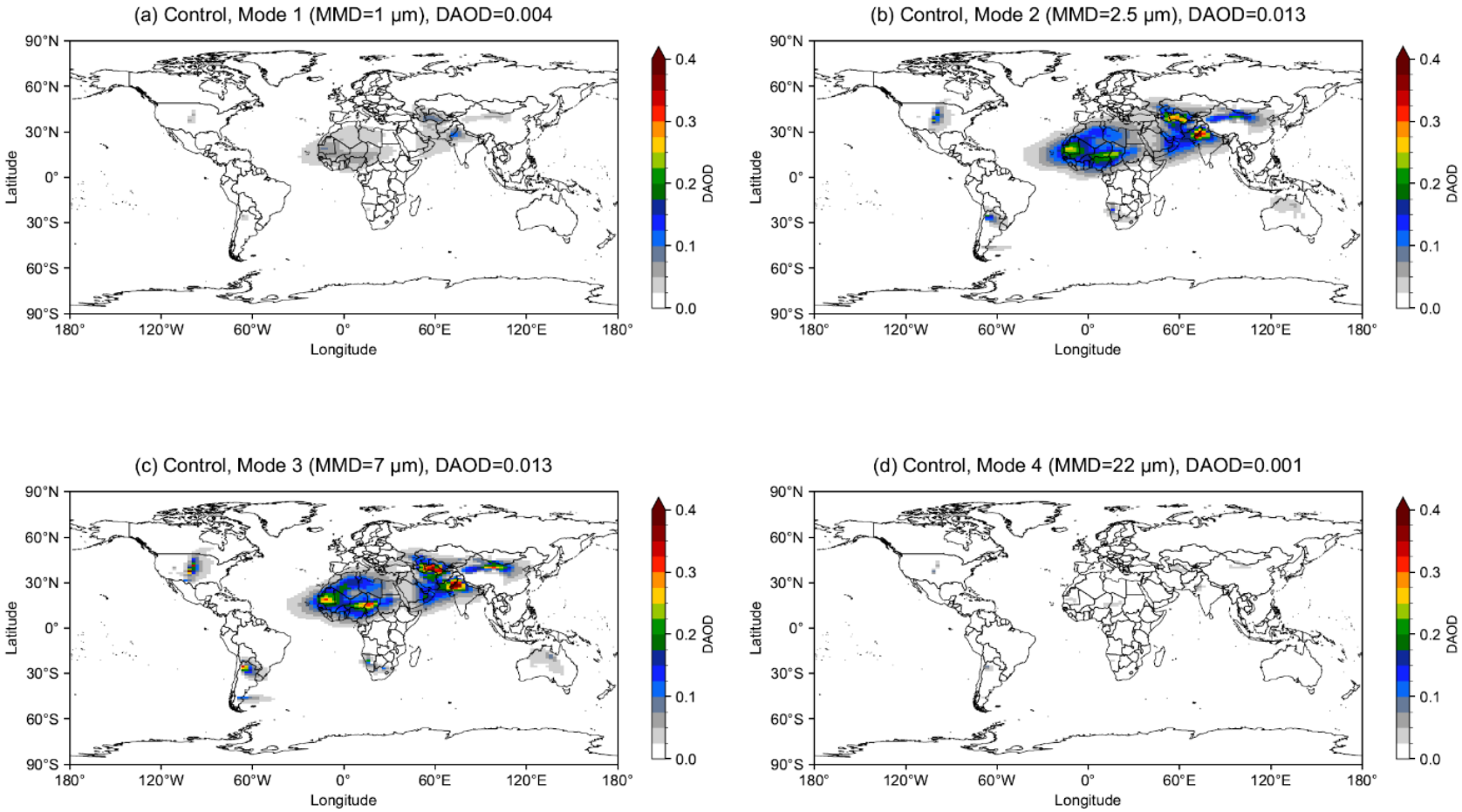

Figure S18. Mean annual Dust Aerosol Optical Depth (DAOD) at 550 nm for individual dust modes in the control simulation in 4-mode configuration. Panels display: (**a**) Mode 1 (1 μm), (**b**) Mode 2 (2.5 μm), (**c**) Mode 3 (7 μm), and (**d**) Mode 4 (22 μm). The scaling coefficients were applied to align with the observation-based target range of 0.030 ± 0.005. The specific area-weighted global mean annual DAOD for each mode is indicated in the respective panel titles. All simulations incorporate scaling coefficients to match the observation-based target range of 0.030 ± 0.005.

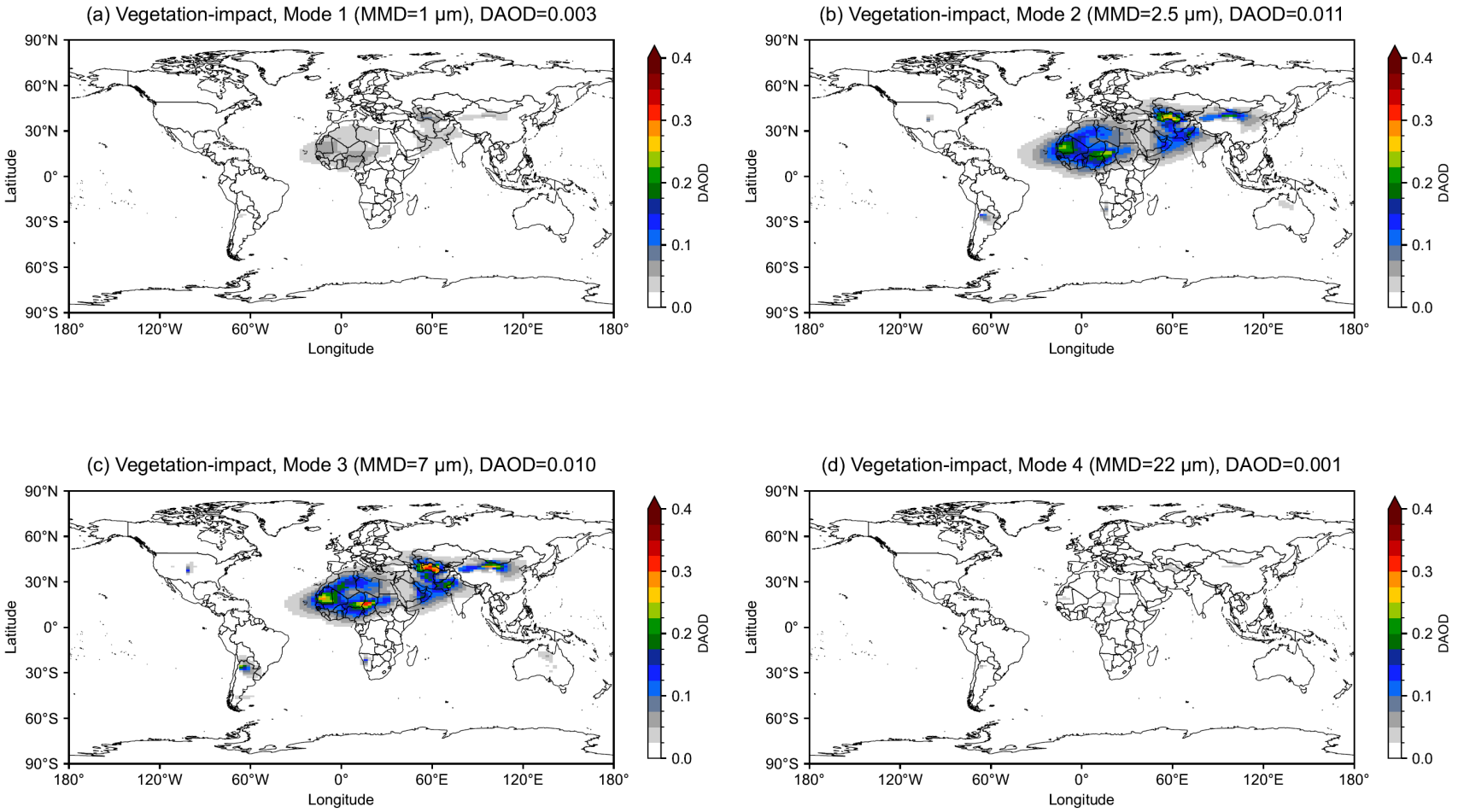

Figure S19. Mean annual Dust Aerosol Optical Depth (DAOD) at 550 nm for individual dust modes in the vegetation-impact simulation in 4-mode configuration. Panels display: (**a**) Mode 1 (1 μm), (**b**) Mode 2 (2.5 μm), (**c**) Mode 3 (7 μm), and (**d**) Mode 4 (22 μm). The scaling coefficients were applied to align with the observation-based target range of 0.030 ± 0.005. The specific area-weighted global mean annual DAOD for each mode is indicated in the respective panel titles. All simulations incorporate scaling coefficients to match the observation-based target range of 0.030 ± 0.005.

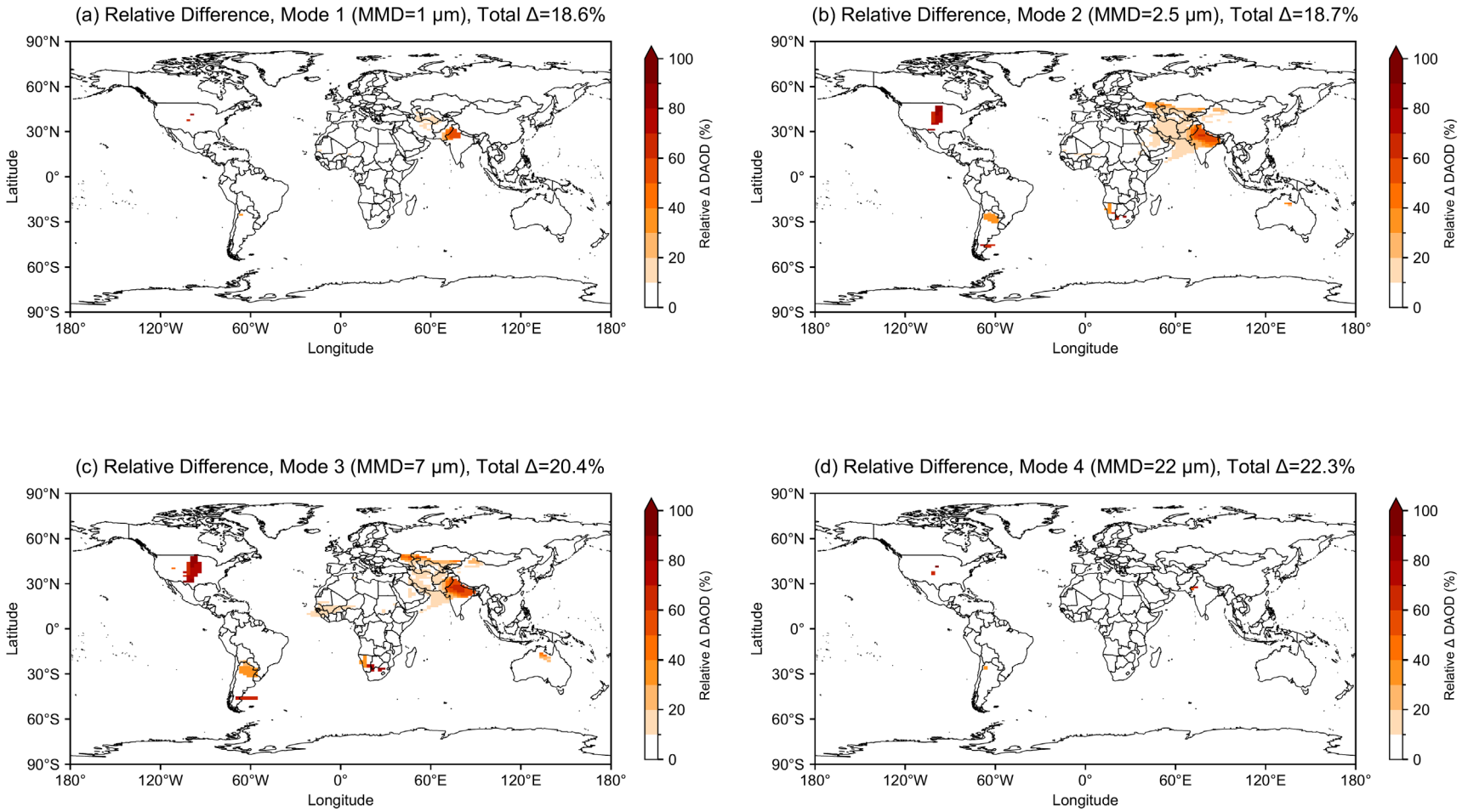

Figure S20. Relative difference of mean annual DAOD at 550 nm for individual dust modes between the control and the vegetation-impact simulation in 4-mode configuration. Panels display: (**a**) Mode 1 (1 μm), (**b**) Mode 2 (2.5 μm), (**c**) Mode 3 (7 μm), and (**d**) Mode 4 (22 μm). The scaling coefficients were applied to align with the observation-based target range of 0.030 ± 0.005. Relative difference of DAOD is calculated as (control minus vegetation-impact) / control, with global total relative difference (Δ) for each mode provided in the respective sub-panel titles. Only grid cells with DAOD in control simulation ≥0.05 are shown. All simulations incorporate scaling coefficients to match the observation-based target range of 0.030 ± 0.005.

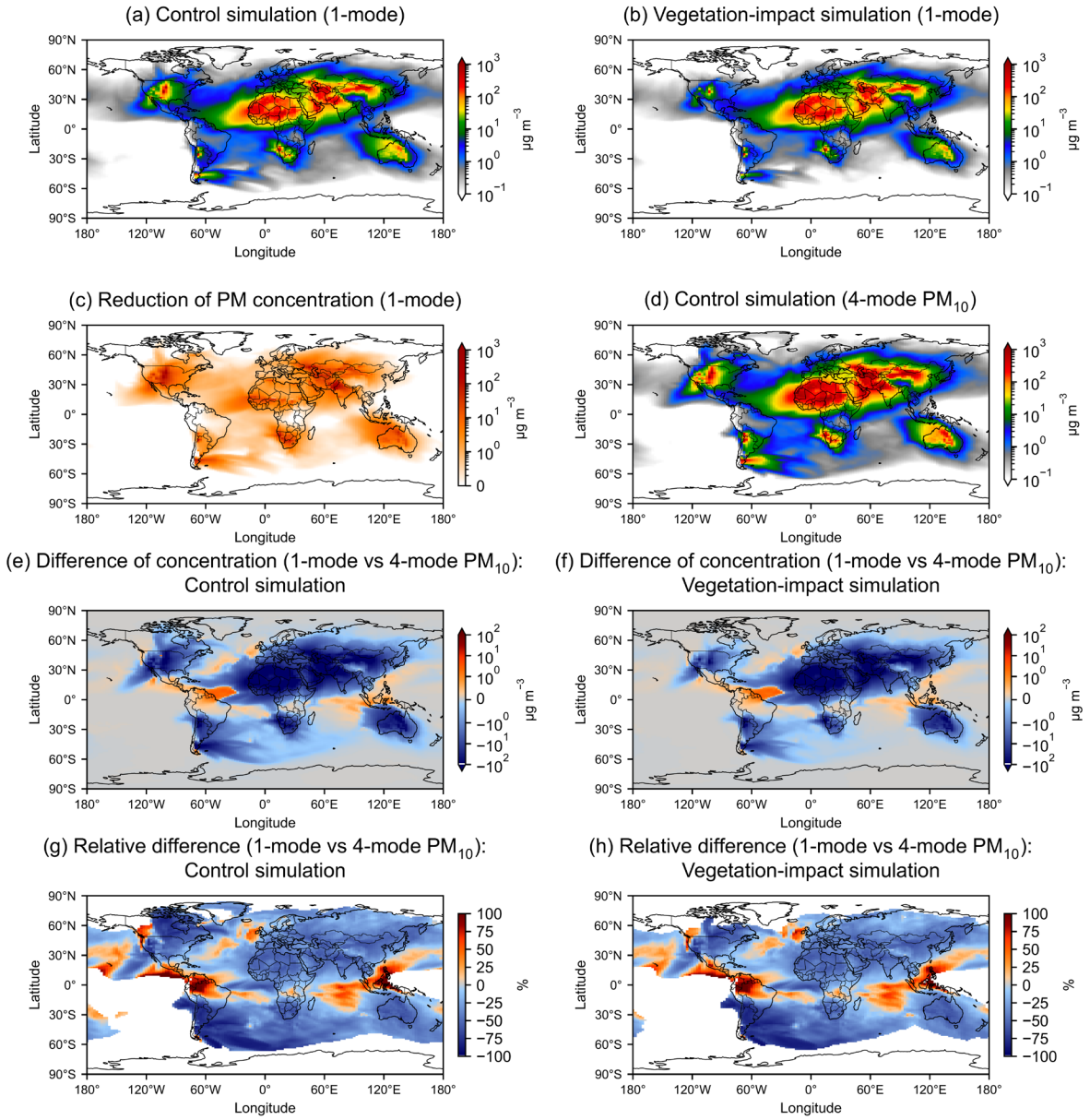

Figure S21. Spatial distribution of mean annual dust surface concentration (μg m^{-3}). Panels (**a**) and (**b**) show the control and vegetation-impact simulations using the 1-mode configuration, respectively. Panel (**c**) shows the reduction in surface concentration between these two 1-mode simulations, calculated as control − vegetation-impact. Panel (**d**) presents the dust surface PM_{10} concentration in the control simulation using the 4-mode configuration. Panels (**e**) and (**f**) show the absolute differences in surface concentration between the 1-mode and 4-mode (PM_{10} component) configurations for the control and vegetation-impact simulations, respectively, calculated as 1-mode − 4-mode PM_{10}. Panels (**g**) and (**h**) show the corresponding relative differences, calculated as (1-mode − 4-mode PM_{10}) / 1-mode.

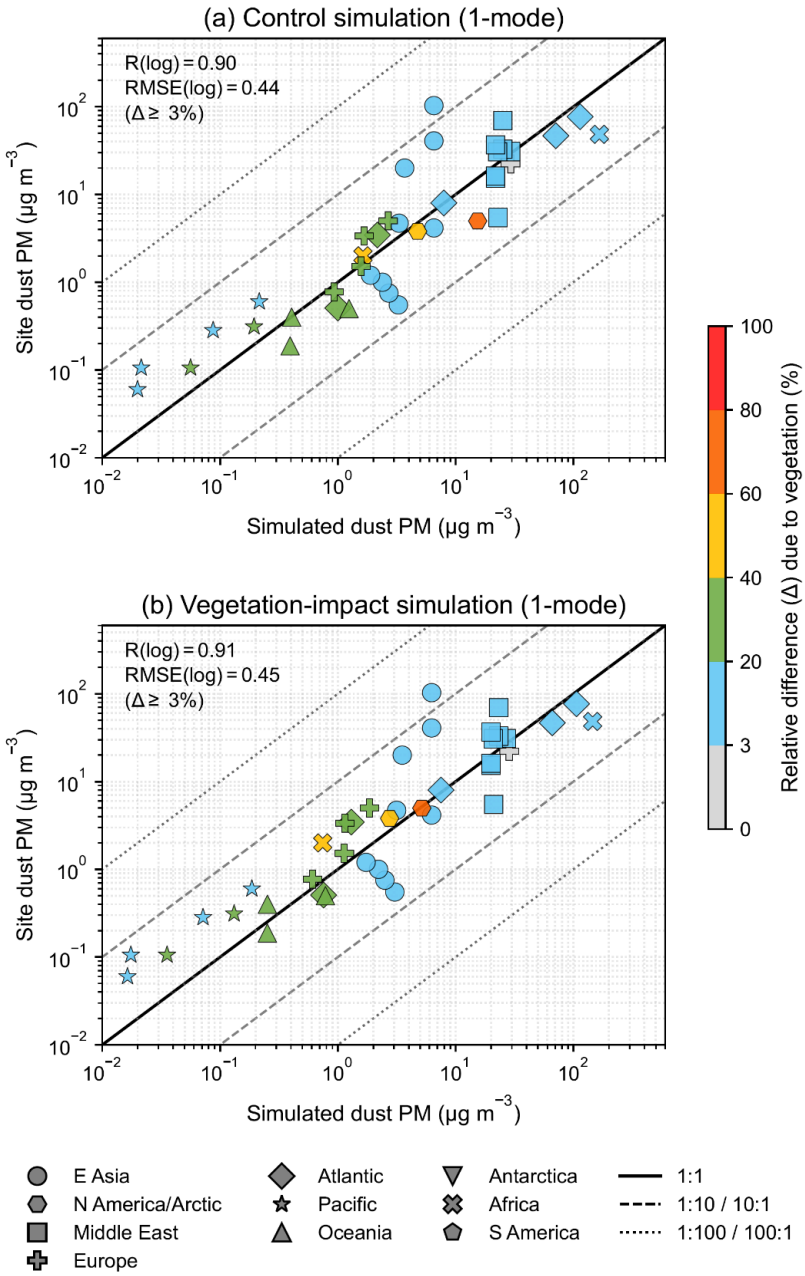

Figure S22. Evaluation of simulated and observed dust surface PM concentration (μg m^{-3}) by Mahowald et al. (2009) in the 1-mode configuration. Panels (**a**) and (**b**) show the control and vegetation-impact simulations, respectively. Both axes are plotted on logarithmic scales. Different regions are indicated by different marker shapes, with colours in each plot representing the relative difference between the control and vegetation-impact simulations. Statistical metrics (R and RMSE, computed in log space) are shown in each panel and are calculated only for data points with relative differences greater than 3 %, highlighting regions sensitive to vegetation impacts. The solid black line denotes the 1:1 relationship. The inner dashed lines indicate the 10:1 and 1:10 ratios, representing simulated values within one order of magnitude of the observations, while the outer dashed lines represent two orders of magnitude (100:1 and 1:100 ratios). Some observational sites are not visible because their values fall below the lower axis limits.

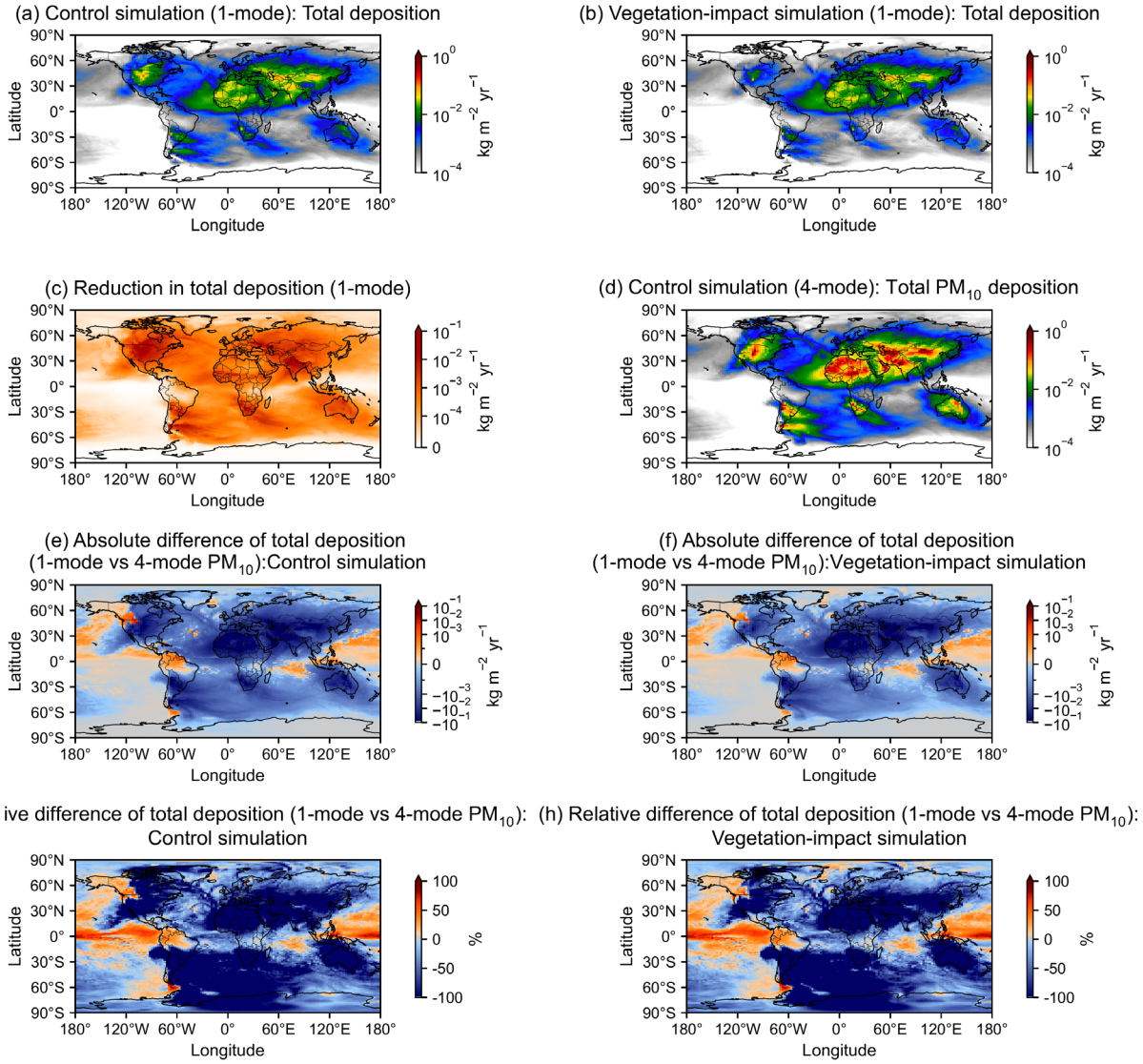

Figure S23. Spatial distribution of mean annual dust surface total deposition (kg m^{-2} yr^{-1}). Panels (**a**) and (**b**) show the control and vegetation-impact simulations using the 1-mode configuration, respectively. Panel (**c**) shows the reduction in surface total deposition between these two 1-mode simulations, calculated as control − vegetation-impact. Panel (**d**) presents the dust surface PM_{10} total deposition in the control simulation using the 4-mode configuration. Panels (**e**) and (**f**) show the absolute differences in surface total deposition between the 1-mode and 4-mode (PM_{10} component) configurations for the control and vegetation-impact simulations, respectively, calculated as 1-mode − 4-mode PM_{10}. Panels (**g**) and (**h**) show the corresponding relative differences, calculated as (1-mode − 4-mode PM_{10}) / 1-mode.

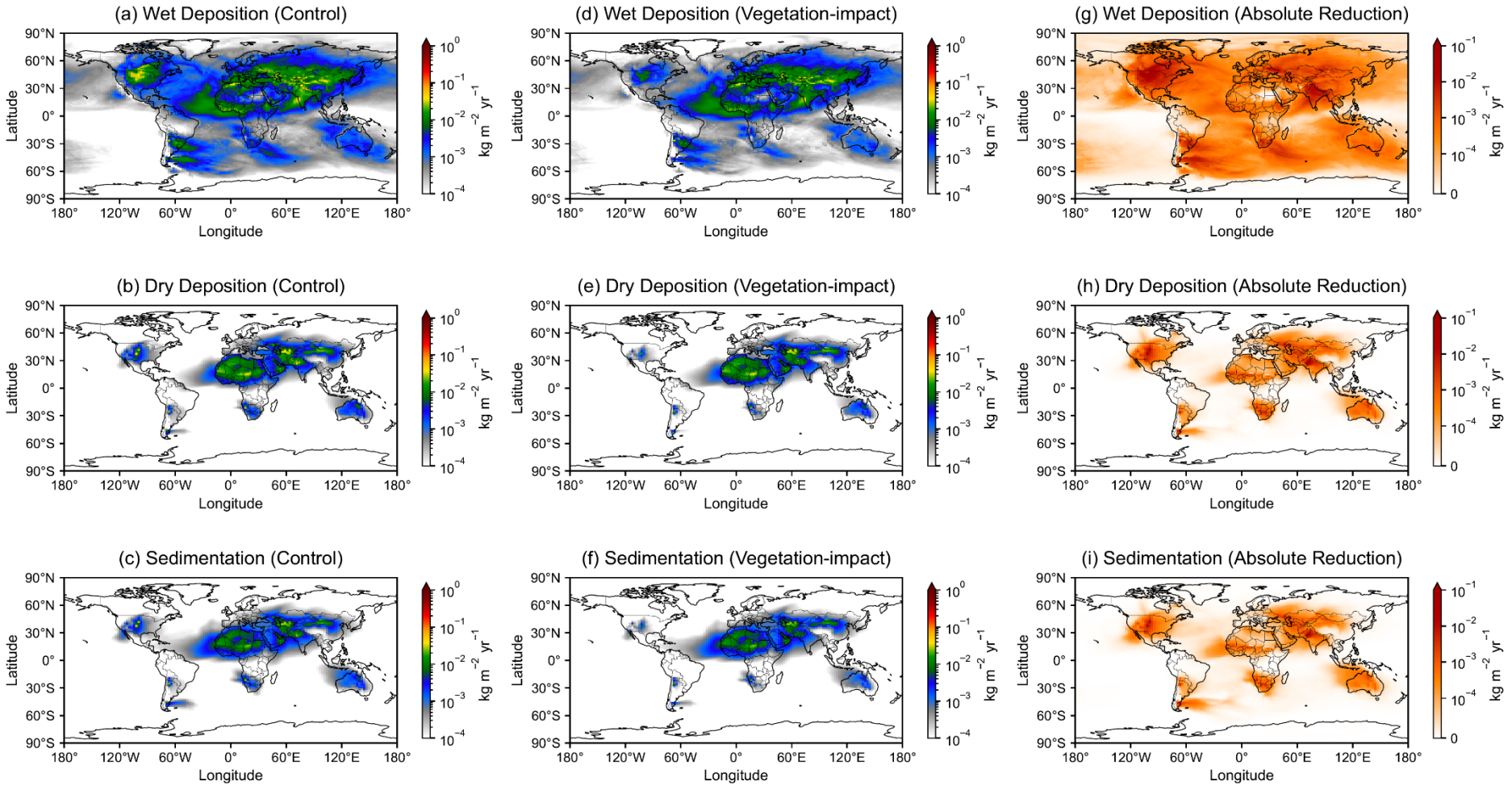

Figure S24. Global dust surface deposition processes (kg m^{-2} yr^{-1}) in the 1-mode configuration. Wet deposition (**a**, **d**, **g**), dry deposition (**b**, **e**, **h**), and sedimentation (**c**, **f**, **i**) are shown for the control (**a**–**c**) and vegetation-impact (**d**–**f**) simulations. The absolute difference (**g**–**i**) is calculated as control − vegetation-impact.

290

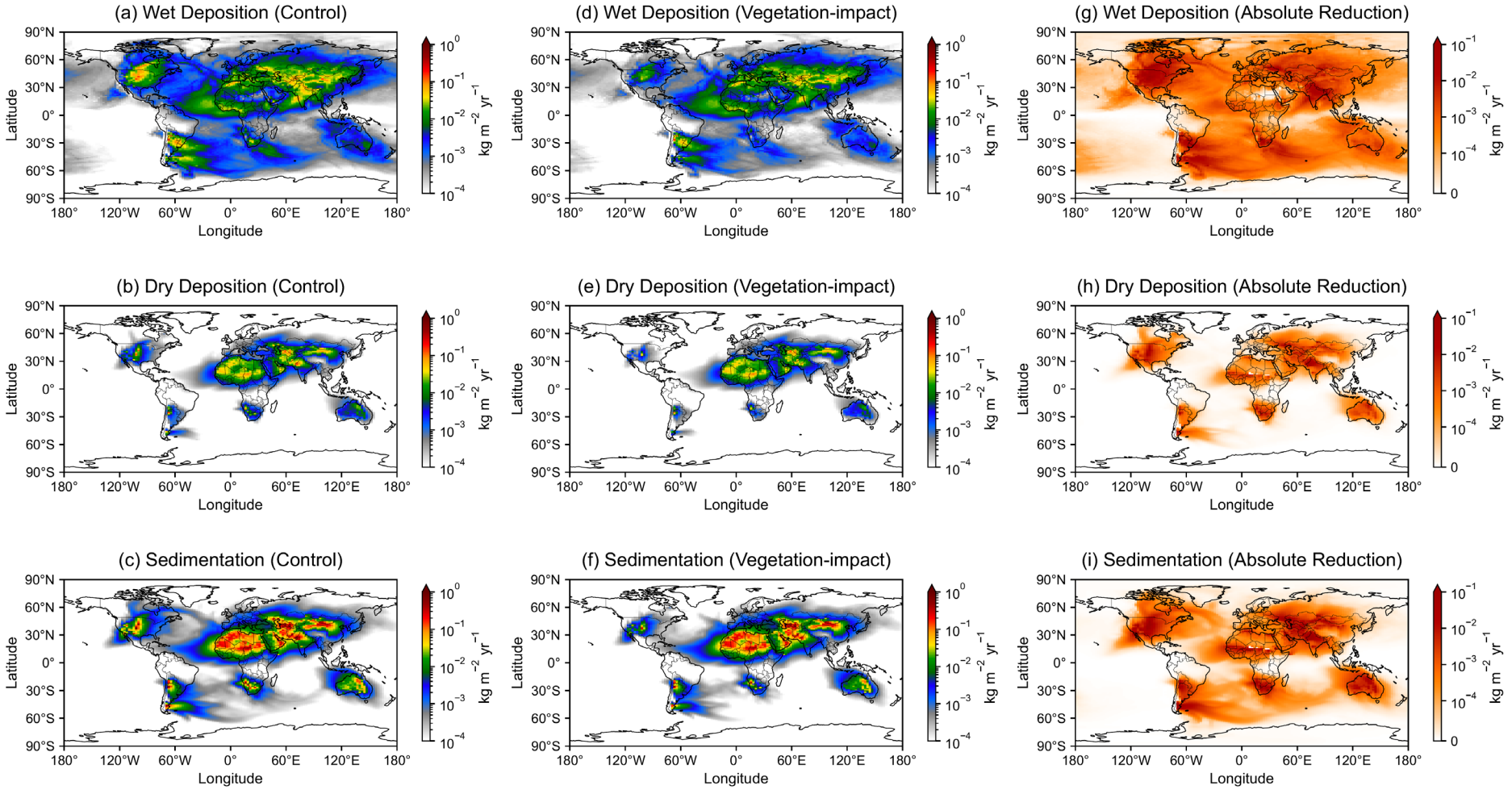

Figure S25. Global dust surface deposition processes (kg m^{-2} yr^{-1}) in the 4-mode configuration. Wet deposition (**a**, **d**, **g**), dry deposition (**b**, **e**, **h**), and sedimentation (**c**, **f**, **i**) are shown for the control (**a**–**c**) and vegetation-impact (**d**–**f**) simulations. The absolute difference (**g**–**i**) is calculated as control − vegetation-impact.

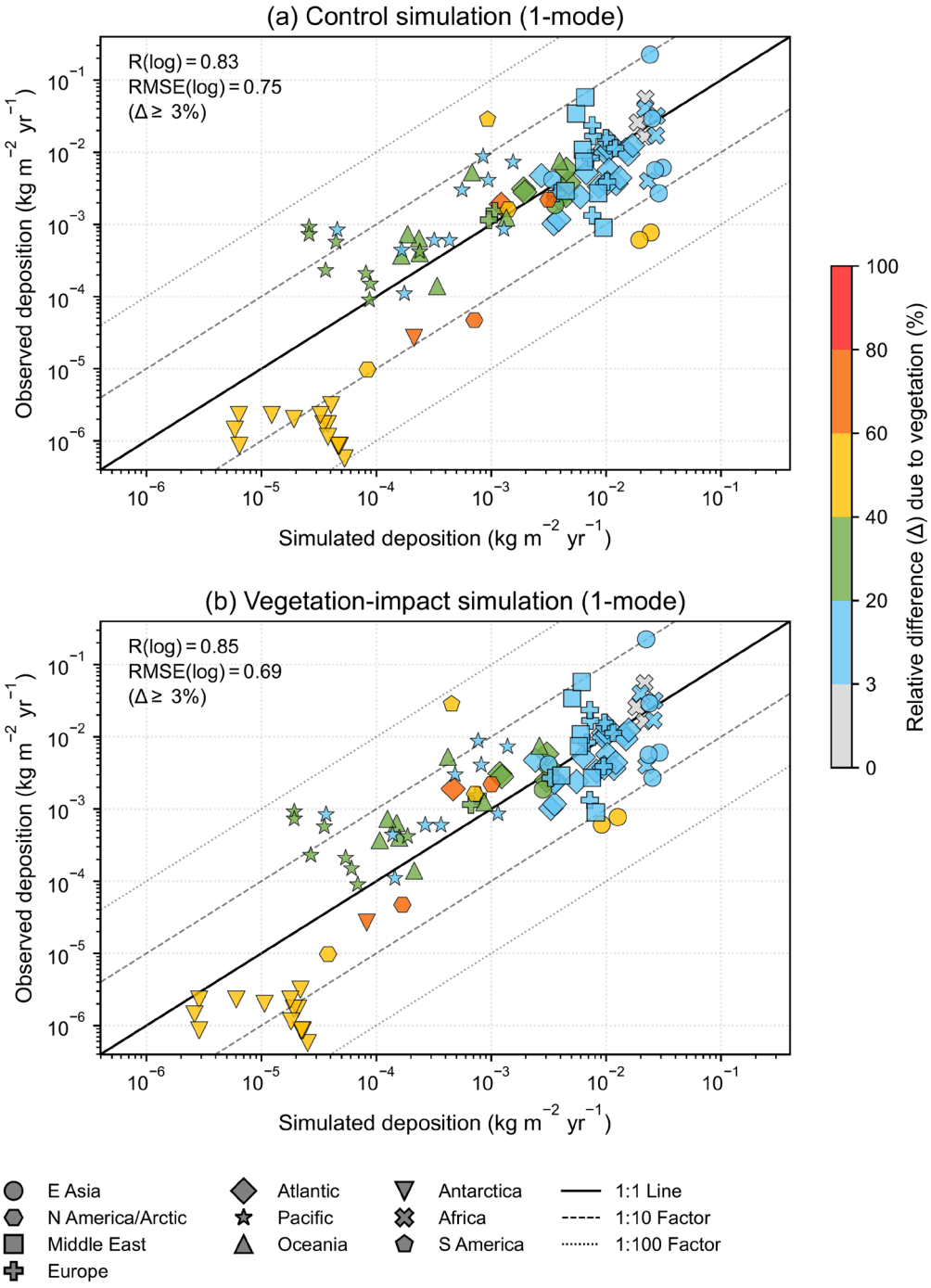

295 **Figure S26**. Evaluation of simulated and observed dust surface PM_{10} total deposition (kg m^{-2} yr^{-1}) by Albani et al. (2014) in the 1-mode configuration. Panels (**a**) and (**b**) show the control and vegetation-impact simulations, respectively. Both axes are plotted on logarithmic scales. Different regions are indicated by different marker shapes, with colours representing the relative difference between the control and vegetation-impact simulations. Statistical metrics (R and RMSE, computed in log space) are shown in each panel and are calculated only for data
300 points with relative differences (Δ) greater than 5 %, highlighting regions sensitive to vegetation impacts. The solid black line denotes the 1:1 relationship. The inner dashed lines indicate the 10:1 and 1:10 ratios, representing simulated values within one order of magnitude of the observations, while the outer dashed lines represent two orders of magnitude (100:1 and 1:100 ratios). Some observational sites are not visible because their values fall below the lower axis limits.

305

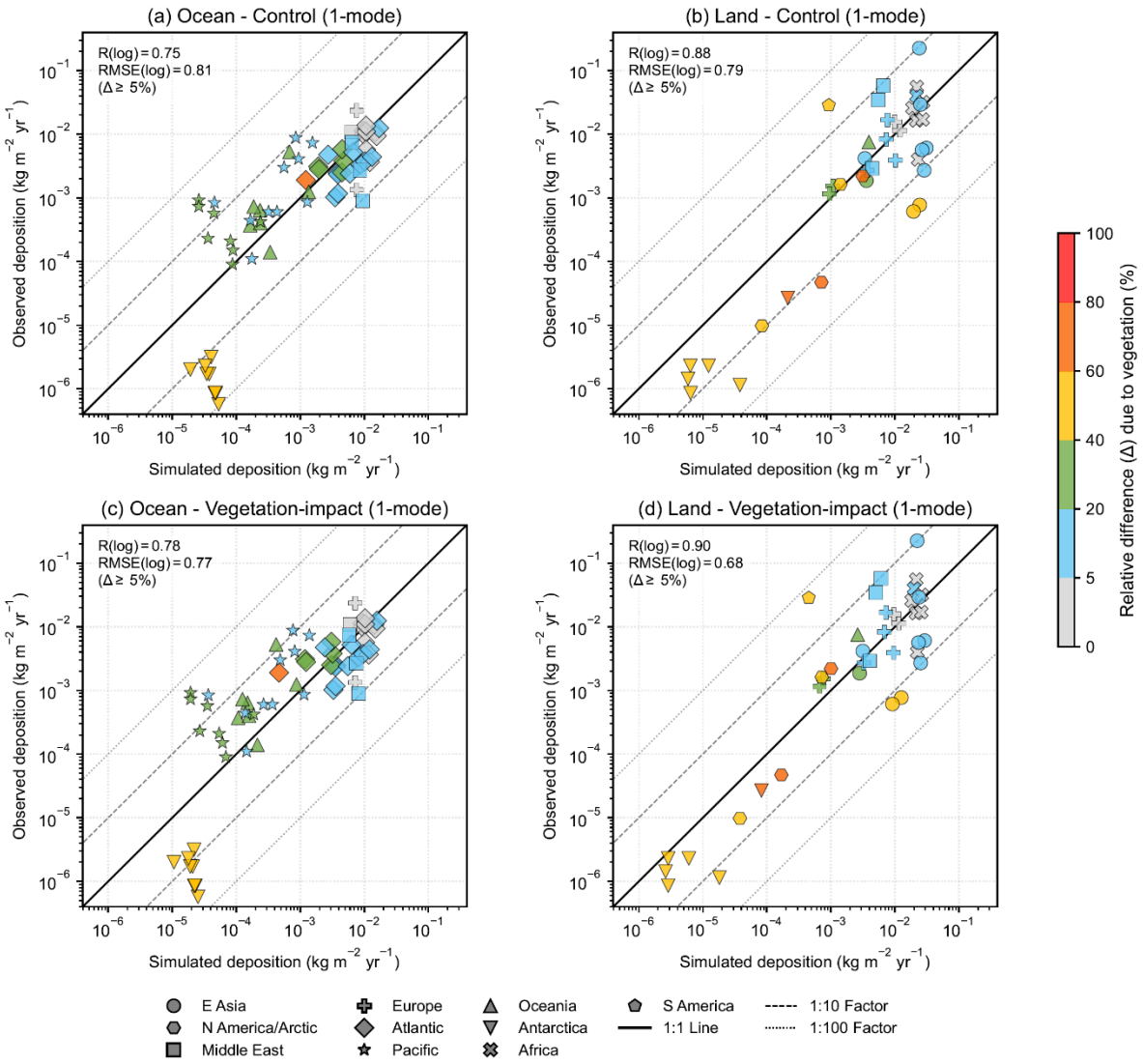

Figure S27. Comparison of simulated dust total deposition (kg m^{-2} yr^{-1}) in the 1-mode configuration with observed dust deposition from Albani et al. (2014), separated into ocean and land sites. Panels (**a**) and (**c**) show ocean points, while panels (**b**) and (**d**) show land points, classified using the NASA land mask. The top row (**a, b**) corresponds to control simulations without vegetation, and the bottom row (**c, d**) to vegetation-impact simulations. Both axes are shown on logarithmic scales. Different regions are indicated by different marker shapes, with colours representing the relative difference between the control and vegetation-impact simulations. Statistical metrics (R and RMSE, computed in log space) are shown in each panel and are calculated only for data points with relative differences (Δ) greater than 5 %, highlighting regions sensitive to vegetation impacts. The solid black line denotes the 1:1 relationship. The inner dashed lines indicate the 10:1 and 1:10 ratios, representing simulated values within one order of magnitude of the observations, while the outer dashed lines represent two orders of magnitude (100:1 and 1:100 ratios). Some observational sites are not visible because their values fall below the lower axis limits.

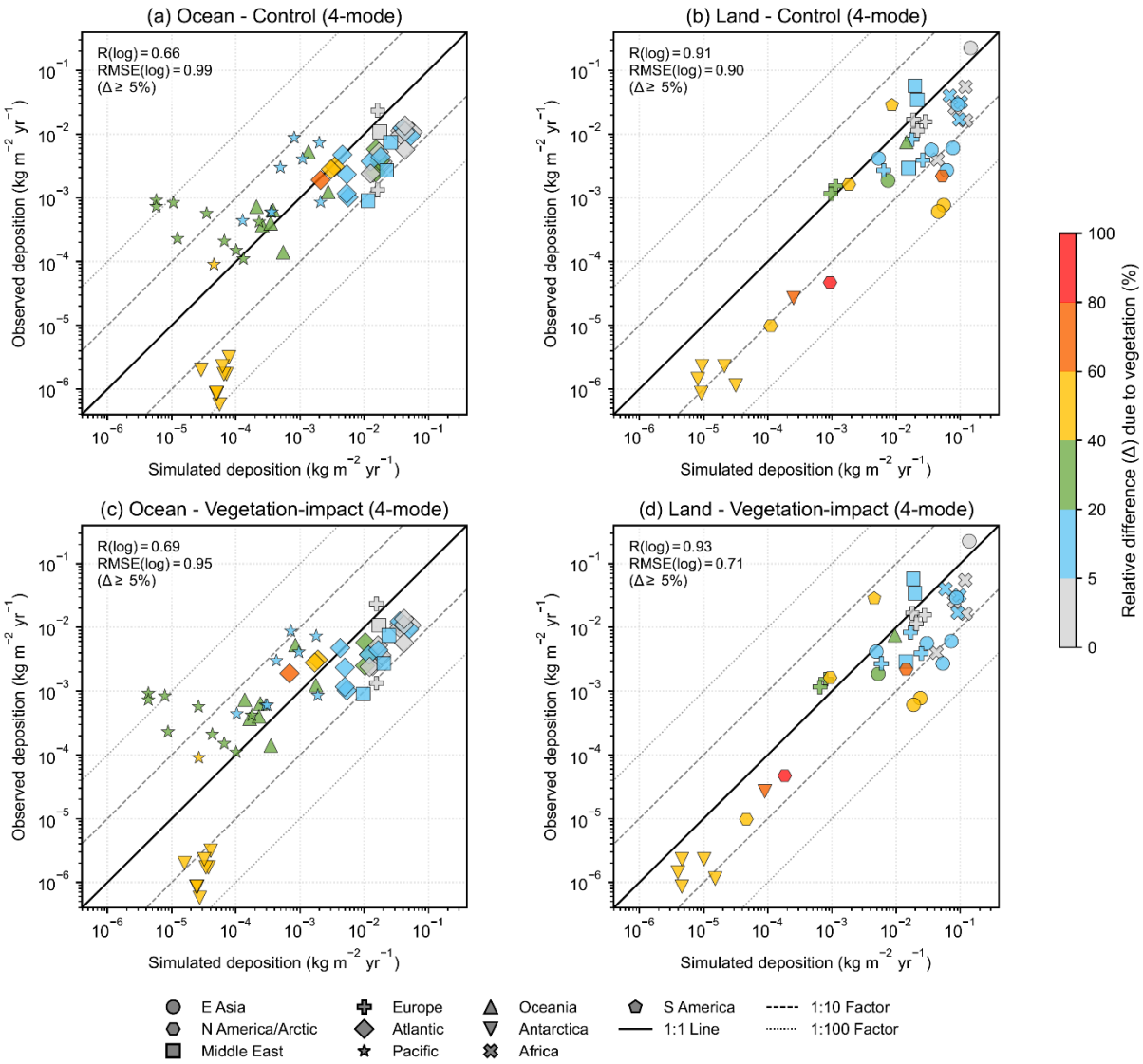

Figure S28. Comparison of simulated dust total deposition (kg m^{-2} yr^{-1}) in the 4-mode configuration with observed dust deposition from Albani et al. (2014), separated into ocean and land sites. Panels (**a**) and (**c**) show ocean points, while panels (**b**) and (**d**) show land points, classified using the NASA land mask. The top row (**a, b**) corresponds to control simulations without vegetation, and the bottom row (**c, d**) to vegetation-impact simulations. Both axes are shown on logarithmic scales. Different regions are indicated by different marker shapes, with colours representing the relative difference between the control and vegetation-impact simulations. Statistical metrics (R and RMSE, computed in log space) are shown in each panel and are calculated only for data points with relative differences (Δ) greater than 5 %, highlighting regions sensitive to vegetation impacts. The solid black line denotes the 1:1 relationship. The inner dashed lines indicate the 10:1 and 1:10 ratios, representing simulated values within one order of magnitude of the observations, while the outer dashed lines represent two orders of magnitude (100:1 and 1:100 ratios). Some observational sites are not visible because their values fall below the lower axis limits.

Reference

Albani, S., Mahowald, N. M., Perry, A. T., Scanza, R. A., Zender, C. S., Heavens, N. G., Maggi, V., Kok, J. F., and Otto-Bliesner, B. L.: Improved dust representation in the Community Atmosphere Model, J. Adv. Model. Earth Syst., 6, 541–570, https://doi.org/10.1002/2013MS000279, 2014.

An, Z., Wu, G., Li, J., Sun, Y., Liu, Y., Zhou, W., Cai, Y., Duan, A., Li, L., Mao, J., Cheng, H., Shi, Z., Tan, L., Yan, H., Ao, H., Chang, H., and Feng, J.: Global monsoon dynamics and climate change, Annu. Rev. Earth Planet. Sci., 43, 29–77, https://doi.org/10.1146/annurev-earth-060313-054623, 2015.

Balkanski, Y., Bonnet, R., Boucher, O., et al.: Better representation of dust can improve climate models with too weak an African monsoon, Atmos. Chem. Phys., 21, 11423–11435, https://doi.org/10.5194/acp-21-11423-2021, 2021.

Bergametti, G., Rajot, J.-L., Marticorena, B., Féron, A., Gaimoz, C., Chatenet, B., Coulibaly, M., Koné, I., Maman, A., and Zakou, A.: Rain, wind, and dust connections in the Sahel, J. Geophys. Res. Atmos., 127, e2021JD035802, https://doi.org/10.1029/2021JD035802, 2022.

Chappell, A., Webb, N. P., Hennen, M., Zender, C. S., Ciais, P., Schepanski, K., Edwards, B. L., Ziegler, N. P., Balkanski, Y., Tong, D., Leys, J. F., Heidenreich, S., Hynes, R., Fuchs, D., Zeng, Z., Baddock, M. C., Lee, J. A., and Kandakji, T.: Elucidating hidden and enduring weaknesses in dust emission modeling, J. Geophys. Res. Atmos., 128, e2023JD038584, https://doi.org/10.1029/2023JD038584, 2023.

Kok, J. F., Adebiyi, A. A., Albani, S., Balkanski, Y., Checa-Garcia, R., Chin, M., Colarco, P. R., Hamilton, D. S., Huang, Y., Ito, A., Klose, M., Leung, D. M., Li, L., Mahowald, N. M., Miller, R. L., Obiso, V., Pérez García-Pando, C., Rocha-Lima, A., Wan, J. S., and Whicker, C. A.: Improved representation of the global dust cycle using observational constraints on dust properties and abundance, Atmos. Chem. Phys., 21, 8127–8167, https://doi.org/10.5194/acp-21-8127-2021, 2021a.

Kok, J. F., Adebiyi, A. A., Albani, S., Balkanski, Y., Checa-Garcia, R., Chin, M., Colarco, P. R., Hamilton, D. S., Huang, Y., Ito, A., Klose, M., Li, L., Mahowald, N. M., Miller, R. L., Obiso, V., Pérez García-Pando, C., Rocha-Lima, A., and Wan, J. S.: Contribution of the world's main dust source regions to the global cycle of desert dust, Atmos. Chem. Phys., 21, 8169–8193, https://doi.org/10.5194/acp-21-8169-2021, 2021b.

Leung, D. M., Kok, J. F., Li, L., Mahowald, N. M., Lawrence, D. M., Tilmes, S., Kluzek, E., Klose, M., and Pérez García-Pando, C.: A new process-based and scale-aware desert dust emission scheme for global climate models – Part II: Evaluation in the Community Earth System Model version 2 (CESM2), Atmos. Chem. Phys., 24, 2287–2318, https://doi.org/10.5194/acp-24-2287-2024, 2024.

Mahowald, N. M., Engelstaedter, S., Luo, C., Sealy, A., Artaxo, P., Benitez-Nelson, C., Bonnet, S., Chen, Y., Chuang, P. Y., Cohen, D. D., Dulac, F., Herut, B., Johansen, A. M., Kubilay, N., Losno, R., Maenhaut, W., Paytan, A., Prospero, J. M., Shank, L. M., and Siefert, R. L.: Atmospheric Iron Deposition: Global Distribution, Variability, and Human Perturbations, Annu. Rev. Mar. Sci., 1, 245–278, https://doi.org/10.1146/annurev.marine.010908.163727, 2009.

Mahowald, N., Ginoux, P., Okin, G. S., Kok, J., Albani, S., Balkanski, Y., Chin, M., Bergametti, G., Eck, T. F., García-Pando, C. P., Gkikas, A., Ageitos, M. G., Kim, D., Klose, M., LeGrand, S., Li, L., Marticorena, B., Miller, R., Ryder, C., Zender, C., and Yu, Y.: Letter to the Editor regarding Chappell et al., 2023, "Satellites reveal Earth's

seasonally shifting dust emission sources", Sci. Total Environ., 949, 174792, https://doi.org/10.1016/j.scitotenv.2024.174792, 2024.

Nan, Y., and Wang, Y.: De-coupling interannual variations of vertical dust extinction over the Taklimakan Desert during 2007–2016 using CALIOP, Sci. Total Environ., 633, 608–617, https://doi.org/10.1016/j.scitotenv.2018.03.125, 2018.

Pope, R. J., Marsham, J. H., Knippertz, P., Brooks, M. E., and Roberts, A. J.: Identifying errors in dust models from data assimilation, Geophys. Res. Lett., 43, 9270–9279, https://doi.org/10.1002/2016GL070621, 2016.

Pu, B., Ginoux, P., Guo, H., Hsu, N. C., Kimball, J., Marticorena, B., Malyshev, S., Naik, V., O'Neill, N. T., Pérez García-Pando, C., Paireau, J., Prospero, J. M., Shevliakova, E., and Zhao, M.: Retrieving the global distribution of the threshold of wind erosion from satellite data and implementing it into the Geophysical Fluid Dynamics Laboratory land–atmosphere model (GFDL AM4.0/LM4.0), Atmos. Chem. Phys., 20, 55–81, https://doi.org/10.5194/acp-20-55-2020, 2020.

Tewari, K., Mishra, S. K., Dewan, A., et al.: Influence of the height of Antarctic ice sheet on its climate, Polar Sci., 28, 100642, https://doi.org/10.1016/j.polar.2021.100642, 2021.

Uematsu, M., Wang, Z., and Uno, I.: Atmospheric input of mineral dust to the western North Pacific region based on direct measurements and a regional chemical transport model, Geophys. Res. Lett., 30, 1342, https://doi.org/10.1029/2002GL016645, 2003.